The photoreaction of TiO2 and Au/TiO2 single crystal and powder surfaces with organic adsorbates. Emphasis on hydrogen production from renewables

ARTICLE *in* GREEN CHEMISTRY · JANUARY 2012

Impact Factor: 8.02 · DOI: 10.1039/C1GC15992E

2 AUTHORS:

Karen Connelly
University of Nottingham
4 PUBLICATIONS **78** CITATIONS
SEE PROFILE

Hicham Idriss
Saudi Basic Industries Corporation (SABIC)
234 PUBLICATIONS **4,723** CITATIONS
SEE PROFILE

Green Chemistry

Cite this: *Green Chem.*, 2012, **14**, 260

www.rsc.org/greenchem

CRITICAL REVIEW

The photoreaction of TiO_2 and Au/TiO_2 single crystal and powder surfaces with organic adsorbates. Emphasis on hydrogen production from renewables

Karen A. Connelly[a] **and Hicham Idriss***[a,b]

Received 11th August 2011, Accepted 26th October 2011
DOI: 10.1039/c1gc15992e

TiO_2 and TiO_2-based materials are prototypes for photo-catalytic reactions as they have been shown for many decades to be active for total oxidation of hydrocarbons to clean the environment. In the last decade or so there has been a shift in the objectives for photoreactions mainly towards hydrogen production from renewables. Here we review the fundamentals behind the reactivity of model TiO_2 surfaces with simple organic compounds in the dark and under photo-irradiation, then we consider the case of ethanol photo-reaction to hydrogen at its fundamental and applied levels. The review starts with an overview of the bulk and surface structures of rutile TiO_2, as it is the most studied phase in surface science despite its lower activity for hydrogen production compared to the anatase phase. We then focus on the gold/TiO_2 system where both phases (anatase and rutile) of TiO_2 have received more attention. In the gold/TiO_2 system emphasis is mainly devoted to understanding the effect of particle dimensions on the electronic conduction as well as the oxidation state of Au particles. The most recent observation using environmental X-ray Photoelectron Spectroscopy indicated the absence of charge transfer from the support to the metal. The photoreaction of ethanol is presented in more detail. The rate for hydrogen production on Au/TiO_2 catalysts does not change if TiO_2 particles are of macro-size or nano-size once normalised by surface area. Also, it was clearly seen that Au/TiO_2 anatase is about two orders of magnitudes higher compared to a similar system where TiO_2 is in the rutile phase. The mechanism for hydrogen production is presented and discussed on the metal/semiconductor systems. Of particular interest is the observation of synergistic effect between the anatase and rutile nanoparticles and one explanation involving electron transfer from one phase to the other is invoked.

1. Introduction

1.1 Drivers for hydrogen production

Hydrogen as an energy carrier has the potential to revolutionise the way in which we meet our energy needs on a global scale. As a fuel, hydrogen boasts great versatility from direct use in internal combustion engines, gas turbines or fuel cells for both distributed heat and electricity generation needs.[1] The main challenge in the harnessing of hydrogen to rival electricity as *the* energy carrier of choice is not related to the abundance of hydrogen available to us, but rather in its lack of natural availability as diatomic H_2 molecules. Due to its high reactivity, hydrogen is more commonly bonded to other elements, for example oxygen and/or carbon, in the form of water and hydrocarbons. The production of hydrogen from these compounds is in contention with the laws of thermodynamics and therefore requires additional energy to break these naturally occurring bonds.[2] The greatest advantage of H_2 as a fuel source is that upon oxidation with either air or oxygen the energy stored within the H–H bonds is released producing only H_2O as the end product.[3] This, combined with the energy value of hydrogen being 122 kJ g^{-1} (around 2.75 times greater than for hydrocarbon fuel combustion), gives clear advantages for the use of hydrogen as a fuel.[4]

Currently the most economically and energetically viable hydrogen production methods are from unsustainable hydrocarbon (natural gas) reforming. However even methane reforming is currently around 4 times more expensive than current methods for producing gasoline with the same energy value.[5] The more integral problem with steam methane reforming is that it is clearly unsustainable in the long term. More sustainable methods, such as those utilising renewable feedstocks such as biomass or water, are presently unfeasible due to economics, incomplete technologies and/or low production yields. However due to the inexhaustible global supply of water, as well as the greater accessibility of biomass to the majority of the population in comparison to hydrocarbons, the benefits of using a purely renewable feedstock for H_2 production has far reaching implications. Although a hydrogen economy is not a new idea, because of the foreseeable depletion of fossil fuels (contributing

[a]*Department of Chemistry, University of Aberdeen, Aberdeen, UK*
[b]*SABIC T&I, Riyadh, Saudi Arabia. E-mail: h.idriss@abdn.ac.uk*

about 80% of the present world energy demand) and associated environmental harms, hydrogen is been viewed as energy carrier for the future. There is also a need to cut down the utilization of fossil fuels because they are responsible for global climate change mainly due to the emission of pollutants including CO_x, NO_x, SO_x, C_xH_y, soot, ash, tars and other organic compounds released into the atmosphere as a result of their combustion. Therefore, increasing focus is being placed on clean energy alternatives. Hydrogen is not a primary energy source, but rather serves as a medium through which primary energy sources (such as nuclear and/or solar energy) can be stored, transmitted and utilized. As an energy carrier, it is especially attractive due to its potential to be used to power chemical fuel cells, although if possible routes are available it is poised to substantially contribute in chemical industry for major chemical compounds such as methanol synthesis, higher hydrocarbons and ammonia. In addition, it is also used as a fuel in rocket engines and as a coolant in some electrical generators. At present hydrogen is produced mainly from fossil fuels, biomass and water.[6]

The methods of hydrogen production from fossil fuels include: steam reforming of natural gas,[7–9] thermal or thermo-catalytic cracking of natural gas,[10–12] catalytic partial oxidation of heavier hydrocarbons[13,14] and coal gasification; such as thermal pyrolysis and supercritical water gasification;[15–22] the methods of hydrogen production from biomass include: steam reforming,[23–25] partial oxidation of ethanol,[26–30] and pyrolysis or gasification[31–36] (which produces a mixture of gases, *i.e.* H_2, CH_4, CO_2, CO, N_2); while the methods of hydrogen production from water are: electrolysis,[37] photolysis,[38] thermo-chemical processes,[39] and biological production.[40]

Among the above-listed processes, nearly 90% of hydrogen is produced by the steam reforming of natural gas or light oil fractions. Coal gasification and electrolysis of water are among other industrial methods for hydrogen production. These industrial methods mainly consume fossil fuel as energy source, and sometimes hydroelectricity. Although the technique of hydrogen production by the steam reforming of natural gas is mature it cannot guarantee long-term strategy for the hydrogen economy because it is neither sustainable nor clean. The hydrogen production through the electrolysis of water is not an energy efficient process as hydrogen obtained through this process carries less energy than the energy input to produce it. Thus, researchers around the world have been focusing on the development of new methods to produce hydrogen from renewable resources. Biomass is considered a renewable energy source because plants store sun energy through photosynthesis process and can release this energy when subjected to an appropriate chemical process, *i.e.* biomass burning. In this way, biomass functions as a sort of natural energy reservoir on earth for storing solar energy.

1.2 Photo-catalysis for hydrogen production

The worldwide availability of solar energy is ~4.3×10^{20} J h^{-1}, with the most advantageous method of optimising the capture, conversion and storage of this energy through the generation of H_2.[3] One approach in achieving this is through the photo-catalytic conversion of a suitable sustainable feedstock; chief among them is water but biomass products such as bio-ethanol have shown to be easier to convert, although as of yet these processes are not financially or energetically viable. TiO_2 as a photo-catalyst for this process has several advantages over other potential photo-catalysts; it is abundant, non-corrosive, has surface stability, is environmentally friendly and is cost effective meaning that its use has greater long-term sustainability than many other photo-catalyst contenders.[41]

Research into the use of TiO_2 as a means for generating hydrogen was initially accelerated by the work of Fujishima and Honda in the 1970s. This work involved photo-catalysis to break down H_2O using an electrochemical cell with a TiO_2 electrode connected to a platinum electrode through an external circuit. Fujishima and Honda found that when the TiO_2 electrode was exposed to UV light a current was established. This was due to the formation of electron-hole pairs, with the current direction

Karen A. Connelly

Karen A. Connelly is a PhD student funded by the Energy Futures Scholarship at the University of Aberdeen. She is currently researching "The dark and photoreactions of ethanol over TiO_2 for the production of hydrogen" using both single crystal and powder samples.

Hicham Idriss

Hicham Idriss has obtained his BSc (1984), MSc (1985), PhD (1987) and habilitation (1997) from the University of Strasbourg (France) and had postdoctoral and research associate positions at the University of Delaware and University of Illinois, Urbana (USA). He joined the Chemistry Department, University of Auckland (New Zealand) in 1995 as a senior Lecturer then became Associate Professor in 2002. In 2008 he moved to the University of Aberdeen (UK) to become Aberdeen Energy Futures Chair and Professor of Chemistry. In 2011 he moved to SABIC (Riyadh) as a chief scientist to work on hydrogen production using solar energy.

indicating that the oxidation reaction occurred at the TiO_2 electrode and the reduction reaction at the platinum electrode.[42] Since then this discovery has led to a proliferation of work conducted in the field of photocatalysis for the intention of hydrogen generation.

Since then many studies were devoted to understand and design photo-catalysts for water splitting to hydrogen and oxygen. A large part of these studies has been compiled in a review in 2009 by Kudo and Miseki.[43] While extracting hydrogen from water is the ultimate objective, research in this direction is still to provide an active and stable photo-catalyst. The reaction of alcohols on the other hand is far easier because alcohols are hole scavengers and therefore higher hydrogen yields are obtained. Among alcohols, ethanol is the most interesting because it is mostly made by fermentation of crops ensuring its renewable cycle. In this review we will first focus on the fundamentals behind the photoreaction, then we will turn our attention to case studies of model surfaces of TiO_2 before presenting the photo-catalytic production of hydrogen from ethanol on real catalytic materials.

The most important semiconductor used for photoreaction is TiO_2. It is also the most understood metal oxide catalyst because its conductivity has allowed over the years spectroscopic and microscopic studies to be conducted. Because of these two reasons, high activity and electronic conductivity, TiO_2 has been the prototype surface for the last two decades or so. Before reviewing some of the photo-catalysis on single crystal TiO_2 surfaces it is worth presenting a brief introduction on the atomic structure of bulk TiO_2 materials.

2.1 Semiconductor atomic structure

There are essentially an infinite number of atoms within a solid and therefore the overlap of individual atomic orbitals and electronic states results in the formation of continuous electronic band structures. This leads to the creation of the valence band (VB) and the conduction band (CB), with the energy level of these bands determining a materials capability of undertaking photo-catalysis.

For a semiconducting transition metal oxide such as TiO_2 the level of these bands is determined by the bonding and anti-bonding behaviour of the electrons within the molecular orbitals (MO) that are formed.[44] The lower energy bonding MOs broaden into the VB, which will be completely filled by electrons at 0 K. The higher energy anti-bonding MOs broadens into the CB, which for d^0 transition metal oxides such as Ti^{4+} in TiO_2, is completely empty at 0 K.[44,45] Between the VB and CB is the bandgap as shown in Fig. 1. The electronic band structure that forms within semiconductors has a bandgap which is small enough to allow for electron excitation from the VB to the CB

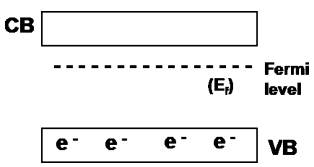

Fig. 1 Schematic diagram of the energy levels of an n-type semiconductor such as TiO_2 at ground state.

through the absorption of photons. The bandgap of rutile TiO_2 is 3.0 eV (400 nm) and therefore a photoreaction involving TiO_2 requires photons with energy equal to or greater than 3.0 eV. In other words, only light with wavelengths of less than 400 nm can provide photons with the necessary energy for photo-excitation in rutile.

Within a semiconductor bandgap lies the Fermi level (E_f) whereby in an ideal semiconductor the density of states (DOS) is zero. At 0 K all energy states below the E_f are occupied by electrons, relating to the highest occupied molecular orbital (HOMO), and energy levels above it are empty, relating to the lowest unoccupied molecular orbital (LUMO).[46] The position of the E_f within the semiconductor bandgap is dependent upon temperature as well as whether the semiconductor is extrinsic or intrinsic. For an n-type semiconductor such as TiO_2 the E_f is found just below the CB minimum, Fig. 1, due to the formation of O vacancies within the bulk introducing occupied energy levels into the otherwise empty band gap. Due to the E_f position being determined by the energy distribution of the electrons it is an important attribute in determining the electrical and thermal properties of the solid.[47]

2.2 Elementary steps for photoreaction over TiO_2

When a photon of adequate energy is absorbed by the catalyst substrate, an electron (e) from the occupied VB gains the required energy to cross the bandgap and move to the CB which was previously empty.[44] The unoccupied electronic state left behind in the VB is now effectively positively charged and referred to as a hole (h). The described photo-catalytic process is shown by eqn (1):

$$TiO_2 + \text{UV photons} \rightarrow e + h \quad (1)$$

The process of photo-excitation in eqn (1) competes with the process of recombination between the newly excited electron-hole pairs. When an electron is photo-excited from the VB to the CB it can diffuse to the surface allowing for charge transfer to an adsorbate or can become trapped within an electron trap in the band gap.[48] If neither of these processes occurs within the excited electron's lifespan, deactivation of the electron-hole pair will occur with the release of either heat or photons. The probability of electron-hole recombination is therefore directly influenced by charge separation and the mobility and lifespan of the electrons and holes. These competing processes are shown in Fig. 2, together with other processes as described in the figure.

In the following we will treat the atomic and electronic structure of rutile TiO_2 as a prototype semiconductor. It is to be emphasised that of the two common polymorphs of TiO_2 (anatase and rutile) the anatase phase is more active for photoreaction in general[43] and in particular for the production of hydrogen from water by photo-electro-chemical methods[49] as well as organic compounds such as alcohols.[50] However in surface science the rutile TiO_2 single crystals (in particular the (110) oriented surface) has received considerable attention and is therefore the most understood. The main reason behind this is the ease by which the rutile phase can be prepared while the anatase phase single crystals are more difficult to make[49] or to obtain naturally with high purity.[51] It is true that in the last few years there has been an emerging interest of TiO_2 anatase single

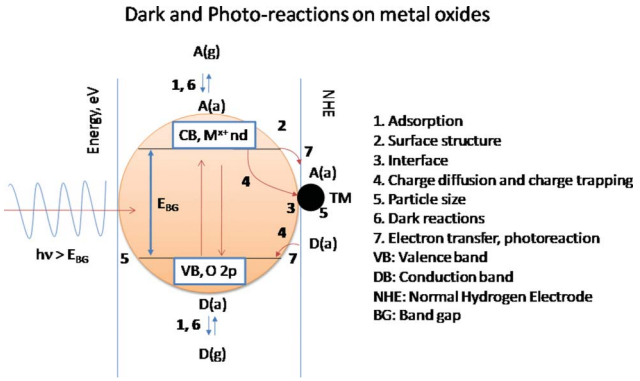

Fig. 2 Representation of the major processes occurring in a semiconductor (with noble metal deposits) following photo-excitation; TM for transition metal.

crystals [ref. 52–54 among others], however none of this work has been applied for the hydrogen production.

2.3 Rutile structure

2.3.1 Bulk structure of rutile. The rutile bulk lattice is tetragonal, consisting of a slightly distorted octahedral formation of titanium (Ti^{4+}) cations surrounded by six oxygen (O^{2-}) anions in with each adjacent octahedra share one O^{2-} anion along the [110] index direction,[55] Fig. 3. In each octahedral configuration the Ti–O bonds at the apices of the octahedron are slightly longer (1.962 Å) than the other Ti–O bonds (1.938 Å) and are stacked so that they alternate by 90° resulting in threefold coordination of the oxygen (O_{3c}) atoms within the bulk structure of rutile.[56,57]

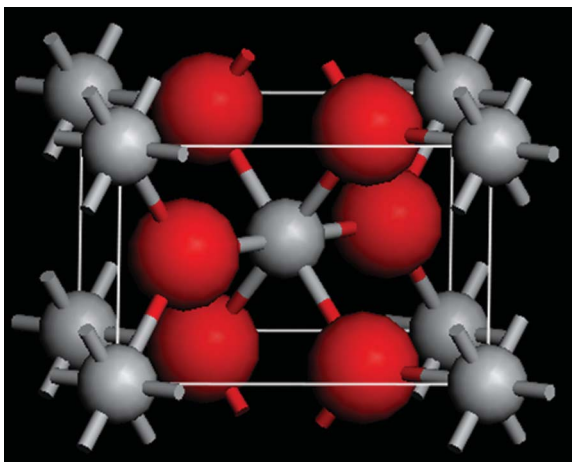

Fig. 3 Bulk structure of rutile TiO_2. Ti cations represented by small grey spheres and O_2^- anions by large red spheres.

2.3.2 Geometric structure of the rutile (110) surface. The rutile (110)–(1x1) surface is the most thermally stable rutile surface and is therefore also the most extensively investigated; the surface structure is shown in Fig. 4. This (110)–(1x1) structure is in agreement with the concepts of both autocompensation and non-polarity.[56] Its surface contains two differently coordinated titanium atoms and two differently coordinated oxygen atoms. Along the [001] crystallographic orientation rows of Ti atoms with sixfold coordination (Ti_{6c}), as seen in the bulk, alternate

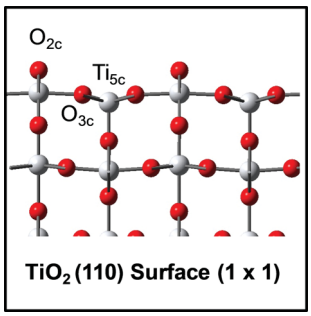

Fig. 4 Ball and stick model of a side view of the relaxed TiO_2 rutile (110) surface with surface atom coordination labelled. Ti cations represented by light gray spheres and O^{2-} anions by red spheres.

with rows of fivefold coordinated Ti (Ti_{5c}) atoms which have one dangling bond at 90° to the surface. Between the Ti atoms within the main surface plane are O_{3c} atoms, as seen in the bulk, whilst twofold coordinated O (O_{2c}) atoms (bridging oxygens) lie in the plane above.[56]

Surface energy (J m^{-2}), governed by the coordinative unsaturation of the surface atoms, has the greatest influence over surface stability and reactivity. The coordination number of rutile (110) surface atoms most closely resembles that of the coordination number of the rutile bulk structure and therefore has the lowest surface energy and greatest surface stability of any of the rutile surfaces.[57–59] Despite the reduced surface reactivity induced by the greater surface stability of the rutile (110) surface in comparison to other rutile crystal orientations it has advantages for use in UHV photocatalytic experimentation as it is thermally stable and does not reconstruct at the elevated temperatures required for crystal annealing.[60]

2.3.3 Electronic structure of the rutile (110) surface. Integral to the reactivity of coordination complexes such as rutile TiO_2 is the part covalent, part ionic nature of the bonding. Bonding arises from the Ti cations interacting with the three lone electron pairs of the O atoms forming coordinate dative covalent bonding.[55] Upon creating the (110) rutile surface the covalent nature of surface bonding arises from autocompensation of the surface creating an excess +4 charge related to the Ti dangling bonds which are neutralised by the –2 charge on the O dangling bonds resulting in an overall charge neutrality of the surface.[55] However the surface bonds also have a strongly ionic character due to electron donation from Ti atoms leading to localisation of charge around the more electronegative O^{2-} anions.[55] This strongly localised charge distribution results in the rutile VB being predominantly occupied with O2p electrons (those in the HOMO) and the CB filled with the empty Ti3d states (those in the LUMO).[45] Within a tetrahedral structure, bonding of Ti with O atoms results in varying degrees of overlap between the differing orientations of the O2p and Ti3d orbitals resulting in orbital hybridisation. The overlap of localised sp^2 hybrids in TiO_2 creates a combination of occupied bonding orbitals and empty antibonding orbitals. Due to the greater electronegativity of the O anions in relation to the Ti cations bonding orbitals are concentrated on the O atom and the antibonding orbitals on Ti atoms.[44]

The presence of O ligands bonded to the Ti centre induces an energy level increase of the Ti3d orbitals and results in

degeneracy of the Ti3d orbitals. The difference in orbital interaction is caused by the differing orientations of the Ti orbitals resulting in a variance in the amount of overlap between them and the ligand orbitals. The splitting of the Ti3d orbitals due to these interactions is known as crystal-field splitting. The octahedral symmetry of TiO_2 has the 6 ligands orientated along the *x*, *y* and *z* axis, as exhibited in Fig. 5. The $d_{x^2-y^2}$ and d_{z^2} orbitals have greatest interaction with the O ligands due to their electron density being concentrated along the *x*, *y* and *z* axes, whilst the d_{xz}, d_{yz} and d_{xy} orbitals have their electron density concentrated between the axes and therefore have less interaction with the ligand orbitals. This is the basis of the creation of two degenerate d-orbitals: a lower energy triply degenerate orbital (t_{2g}) and a higher energy doubly degenerate orbital (e_g).[61] Due to the Ti e_g orbitals pointing directly towards neighbouring O p_x and O p_y orbitals, hybridised covalent σ bonds are formed between them, whilst the t_{2g} orbitals point between neighbouring O p_z orbitals and therefore form weaker π bonding as shown in Fig. 5.[62]

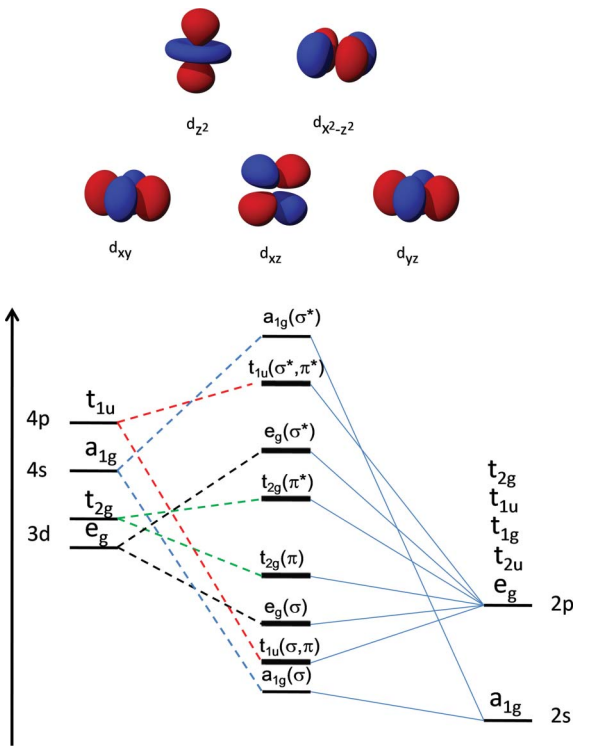

Fig. 5 Molecular orbital diagram of an octahedral complex such as TiO_2 exhibiting the degeneracy of the Ti3d orbitals and the level of orbital hybridisation between Ti and O orbitals with the orientations of the Ti3d orbitals illustrated above. Taken from ref. 62.

The hybridisation contribution of the O2p and degenerate Ti3d orbitals to the bulk DOSs for TiO_2 is shown in Fig. 6.[63] It can be seen from the calculated DOS that the CB is dominated by Ti3d orbitals and the VB by O2p orbitals with a band gap between them where the DOS is zero. However there is some hybridisation or covalent mixing of these Ti and O energy levels in the VB which is seen to be greater in the lower energy bonding part than the upper non-bonding part,[44] The degree of hybridisation of the Ti–O orbitals has been determined using resonant photoemission by tuning the

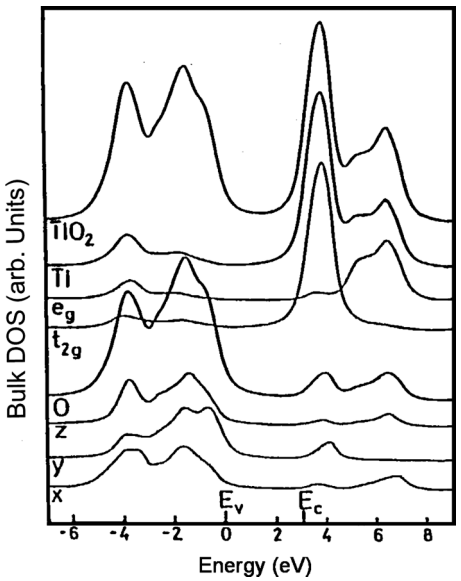

Fig. 6 Bulk DOS of TiO_2 calculated from partial O and Ti DOSs. The $O_{z,y,x}$ DOS contributions are shown individually as well as the individual Ti e_g and t_{2g} contributions. Taken from ref. 63.

photon energy through the Ti 3p → 3d optical absorption edge. Resonant photoemission was observed for the O2p orbitals from this process indicating that there is a strong degree of metal-cation orbital hybridisation,[64] The presence of either defects or impurities introduced by doping can have an extensive effect on the surface electronic structure.

2.3.4 Electronic states of defects. In its stoichiometric form the rutile phase of TiO_2 is an insulating material. However reducing the rutile surface leads to the formation of oxygen deficiencies, decreasing the atomic coordination numbers and therefore adjusting the electron count, resulting in a semi-conductive material and allowing for adsorption to occur at these defect sites, if the acceptor levels allow.[65,66] Naturally occurring rutile is almost always in a reduced state but more controlled defect surface coverage can be produced either by thermal annealing at sufficiently high temperature or through electron bombardment.[67] There are a variety of surface point defect types that can be created on the rutile surface such as doubly charged oxygen vacancies, as well as extended defects such as steps, ridges, terraces and crystallographic shear planes.[56,68,69] The presence of these defects affects local composition and charge as well as modifying the coordination number of adjacent atoms. These alterations consequently result in localised changes of electron density and modify the electronic DOSs in the bandgap.[67,70]

The defects of primary concern for surface adsorption/desorption reactions are oxygen vacancies (O_v). The extent of O_v coverage is considerably dependent upon the reduced state of the crystal bulk.[65] The rutile (110) surface has a maximum defect coverage concentration of around 10% after which the surface begins partially reconstructing.[68] Surface O_v defects can be created at either bridging oxygen sites, as shown in Fig. 7, or at planar oxygen sites, however bridging oxygen defects are created more easily due to the lower degree of atomic coordination that they have.

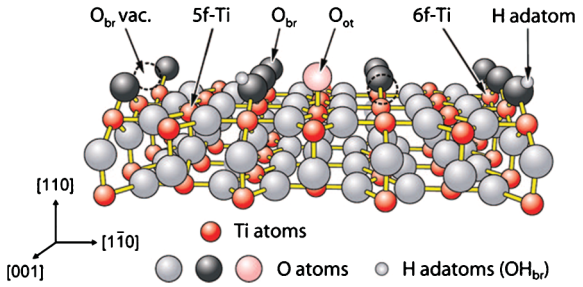

Fig. 7 Ball and stick model of the TiO_2 rutile (110) surface with bridging O_v defects shown. Ti cations represented by small red spheres and O^{2-} anions by large grey (in-plane), black (bridging oxygen) and pink (oxygen adatom) spheres. Taken from ref. 74.

The presence of surface O_v defects is accompanied by the introduction of associated electronic defect states. The two excess electrons from the O_v occupy the empty Ti3d derived states at the bottom of the CB therefore pushing the E_f up to the CB edge. These altered electronic states result in neutralising the charge within the semiconductor as well as acting as charge carrier traps.[55,71–73] The introduction of energy states associated with O_v defects into the band gap is observed in the angle-integrated UPS spectra in Fig. 8 for the stoichiometric and reduced (110) surface. The broad peak between 3.5 and 9.5 eV below the E_f represents the O2p dominated VB with the peak at around 7.5 eV corresponding to the bonding orbitals and the 5.5 eV peak corresponding to the non-bonding orbitals which are observed for both the stoichiometric and reduced structure. For the reduced surface a second peak area around 1 eV below the E_f is observed which corresponds to O_v defect creation and is shown to have a Ti3d derived nature due to the excess –2 charge occupying the previously empty Ti3d orbital.[64]

The increase in surface reactivity observed as a consequence of O_v defect formation is due both to producing sites with lower coordination as well as from the alteration of the electron count by two electrons.[55] The exact mechanism for the increased surface reactivity observed due to oxygen deficiency is still debated. It has been suggested that the –2 excess charge remains at the O_v site creating helium-type donor states, however this theory is now largely disregarded;[55] that the excess –2 charge is accommodated as a localised electron charge spread out over the near area of the O_v site and resulting in the two closest Ti^{4+} cations to be reduced to Ti^{3+}, or more recently it has been suggested that the O deficiency arises from interstitial Ti.

The most recent theory attributing the Ti3d defect band gap state to near surface interstitial Ti cations rather than O_v defects or bridging hydroxylates was proposed by Wendt *et al.* using STM and UPS on stoichiometric, reduced and hydroxylated rutile (110) surfaces. This work stemmed from observations that Ti interstitials in reduced TiO_2 undergo diffusion to the crystal surface upon oxygen exposure at increased temperatures.[74] Wendt *et al.* found that on the (110) rutile surface the gap state originally attributed to bridging O_v defects was not altered after the vacancy had been removed by oxygen adsorption and therefore proposed that this gap state must originate from extra interstitial Ti atoms at the near surface. Furthermore they observe an oxygen dissociation channel associated with surface Ti troughs rather than with the O_v defects. Based on these observations it was proposed that near-surface Ti interstitials must influence the crystal surface and their redox interactions with adsorbates due to the provision of electronic charge from Ti interstitials for oxygen adsorption and desorption.[74]

A number of other studies determined that the Ti3d defect band gap state *is* attributable to O_v defects as proposed by Petrik *et al.* using STM, TPD and electron stimulated desorption (ESD).[69] For these experiments electron bombardment was used rather than thermal annealing so as to control the surface defect coverage whilst keeping the concentration of subsurface Ti^{3+}

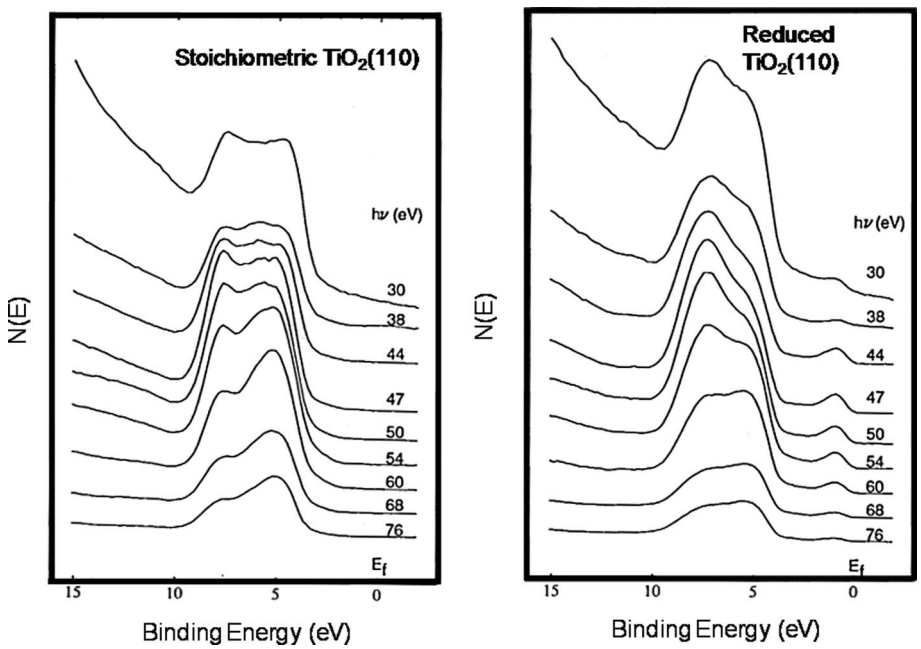

Fig. 8 Series of angle integrated UPS spectra taken for photon energies between 30 and 76 eV for both the stoichiometric and reduced TiO_2 (110). Taken from ref. 64.

interstitials constant. These results showed that the amount of adsorbed molecular O_2 is closely related to the amount of surface defects. This indicates that the surface reactivity in relation to O_2 is fundamentally controlled by electron-donating species such as O_v defects, rather than subsurface Ti^{3+} interstitials.[75] Yim *et al.* are also in agreement with an O_v-related Ti3d band gap defect state by using STM and UPS and also creating defect sites with electron bombardment. The UPS data gives a clear indication that the population of the Ti3d defect band gap state is directly dependent upon the concentration of bridging O_v defects.[76]

2.4 Au/TiO_2

Photo-production of hydrogen from ethanol over the clean rutile TiO_2 surface has not been sufficiently efficient, indicating that hydrogen ion reduction and hydrogen-hydrogen recombination rates are weak on this semiconductor surface[2] unlike photo-oxidation processes.[77] The introduction of transition metals such as Au nanoparticles (NPs) dispersed on the TiO_2 surface has been found to increase reaction efficiency by inhibiting electron-hole recombination, as shown in Fig. 9, and reducing the over-potentials for the generation of H_2.[78] Whether the photocatalytic properties of supported metal NP's on TiO_2 are more critically dependent upon the Au particle morphology such as the size, shape and thickness of the NPs or due to support effects such as charge transfer is still open to debate.[79,80] A detailed study of the effect of both the polymorph of TiO_2 (anatase or rutile) and the effect of Au particle size was also studied.[50] It was found that the rate of hydrogen production from ethanol Au particles of similar sizes deposited on TiO_2 anatase is two orders of magnitudes higher than that on TiO_2 rutile. The reason is invoked as due to electron-hole recombination rates (the electron-hole recombination rate is far slower on TiO_2 anatase compared to that on TiO_2 rutile and therefore there are more excited electrons available to be transferred from the conduction band to the Au particles, which are then transferred to the hydrogen ions in the case of TiO_2 anatase). It was found that the rate of hydrogen production normalised to the amount of available surface Au is not dependent on their particle size in the 3–12 nm range. Of course the same rate decreases when the particle size further increase but this common to catalytic reactions involving both the support (in this case TiO_2) and a transition metal.[50]

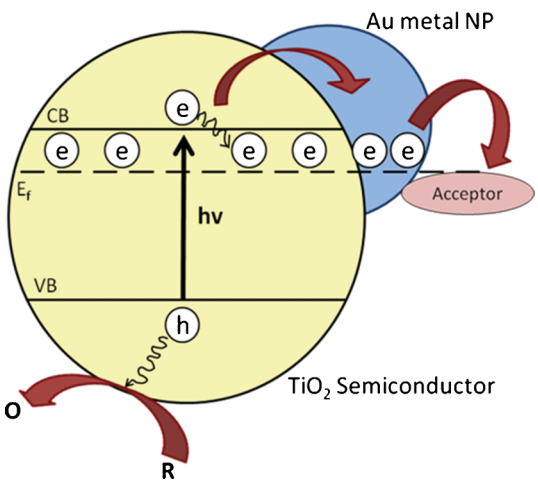

Fig. 9 Enhancement of photo-excitation due to Au NPs acting as electron acceptors. Adapted from ref. 78.

2.4.1 Size effects of Au NPs on TiO_2. Initial work by Haruta *et al.*[81] ascertained that highly dispersed Au NPs on reducible metal oxide supports showed greater enhancement of particular catalytic reactions than for larger sized deposits of gold. In their work[81] it was found that Au deposited by a variety of methods (including vapour deposition) resulted in hemispherical NPs with those of <5 nm diameter found to optimise the catalytic activity of various surface reactions. Valden *et al.*[82] investigated this particle size effect by measuring the surface oxidation reaction of CO over the Au dispersed TiO_2 surface with Au NP sizes ranging from 1–6 nm. It was found that Au NPs of 3.5 nm in size induced maximum enhancement of the surface reaction with only very little enhancement of the reaction observed for NPs of 6 nm, as observed in Fig. 10a. Scanning Tunnelling Spectroscopy (STS) was used to calculate the variation in band gap with Au cluster diameter by measuring the tunnelling current as a function of the bias voltage, as shown in Fig. 10b. The band gap measured for 3.5 nm NPs is between 0.2–0.6 eV with corresponding topographic scans showing a 2 atom layer 3D cluster structure. For NPs of <2 nm diameter larger band gaps up to ~1.4 eV were measured with mostly a 2D layer topography and NP clusters with diameters >5 nm exhibited metallic properties with no band gap states observed. The authors attributed these observations to quantum size effects and proposed that NP thickness may be the key mechanism for enhanced reactivity due to a metal to non-metal transition.

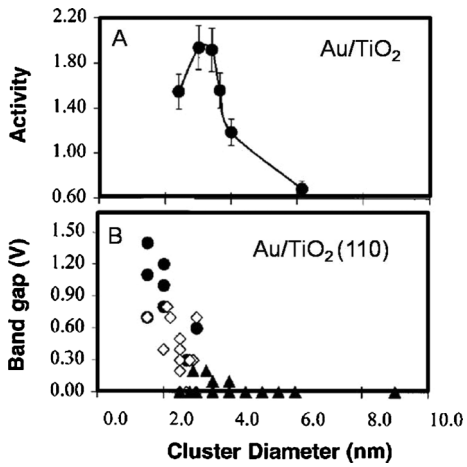

Fig. 10 (a) CO oxidation activity as a function of Au cluster size on TiO_2, (b) cluster band gap as a function of Au cluster size on TiO_2, represents 2D clusters, represents 3D clusters two atom layers in height and represents 3D clusters with three atom layers or greater in height. Taken from ref. 82.

Lai *et al.*[83] replicated the observed enhancement of Turn Over Frequency (TOF) of the CO oxidation reaction for both precipitation synthesized and vapour deposited Au NPs of ~3 nm in size, as shown in Fig. 11.

Using TiO_2 powder Subramanian *et al.*[80] provided evidence for E_f shifts toward the CB in the Au/TiO_2 system corresponding

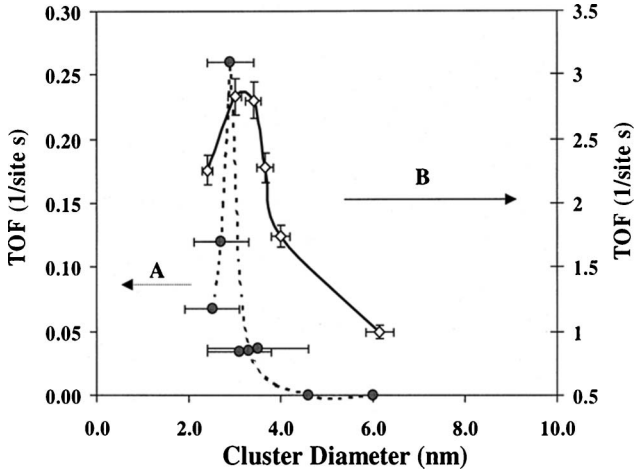

Fig. 11 Turnover frequency (TOF) of CO oxidation as a function of Au cluster size on the TiO_2 surface. The Y axis on the left hand side is for Au deposited on powder TiO_2 and Y-axis on the right hand side is for Au deposited on TiO_2(110) rutile surface. Taken from ref. 83.

favourably with decreasing Au particle size. The redox couple for C_{60}/C_{60}^- was used as a probe for determining the E_f of the semiconductor. A mixture of known TiO_2 and Au NPs were irradiated with UV light with a known amount of C_{60} added to the suspension. Upon equilibration of the C_{60}/C_{60}^- redox couple with the TiO_2 system the apparent E_f for the Au/TiO_2 suspension was determined with varying Au NP size. The E_f determined for TiO_2 alone was –230 mV, with the addition of Au NPs increasing the negativity of the E_f to –250 mV for 8 nm Au, –270 mV for 5 nm Au and –290 mV for 3 nm Au. The calculated increase in negativity moves the E_f closer to the CB due to the greater accumulation of electrons at the Au NPs, as shown in Fig. 12. Upon UV irradiation electrons are excited into the TiO_2 CB and transferred to the Au NPs until equilibrium is reached. As the Au E_f is raised to a more negative potential the resultant composite E_f moves towards the CB of the semiconductor. This composite system is therefore more reductive than TiO_2 alone and improves the photocatalytic reactivity of the semiconductor.

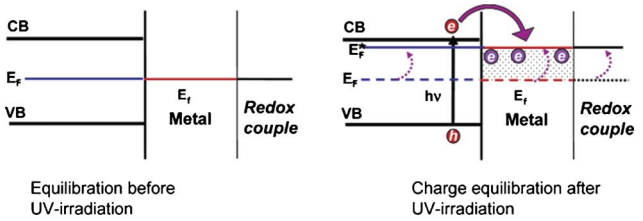

Fig. 12 Schematic of the equilibration of TiO_2 and Au NPs with the redox couple before and after UV irradiation. Taken from ref. 80.

2.4.2 Binding sites of Au NPs on TiO_2. Defect sites are known to play an important role in the nucleation and growth of Au NPs on the rutile surface. The UPS spectra in Fig. 13 show a peak at around 0.9 eV below the E_f, representing the defect energy state associated with reduced Ti^{3+} cations produced from the removal of a bridging oxygen. The second UPS spectrum confirms that the 0.9 eV peak belongs to this defect state as it is removed with increased exposure to O_2. The first spectrum demonstrates that with increased Au coverage the Ti^{3+} peak is suppressed indicating that Au deposition on the reduced rutile surface initially occurs by nucleation at O_v defects and suggesting that bonding between Au and Ti^{3+} has occurred.[84] The donation of excess electron density from the reduced rutile surface to Au NPs is therefore considered to be the main mechanism for the greater binding energy of Au onto the reduced surface in comparison with the stoichiometric surface.[85]

Differences in the binding energy of Au NPs on the reduced rutile surface were observed when varying the Au surface coverage, with higher surface coverage crudely correlated to an increase in the mean NP cluster radius. Jiang *et al.* used direct XPS evidence to conclude that charge transfer from the reduced TiO_2 surface to Au clusters does play a crucial role in core level binding energy.[86] In this work varying amounts of Au were deposited on both stoichiometric and reduced TiO_2 (110) surfaces and XPS Au $4f_{7/2}$ signals measured for each Au surface coverage. On the stoichiometric surface a downward core level binding shift with increased surface coverage of Au was observed, as shown in Fig. 14. The authors indicate that this is due to particle size effects.[87] For the reduced surface the same

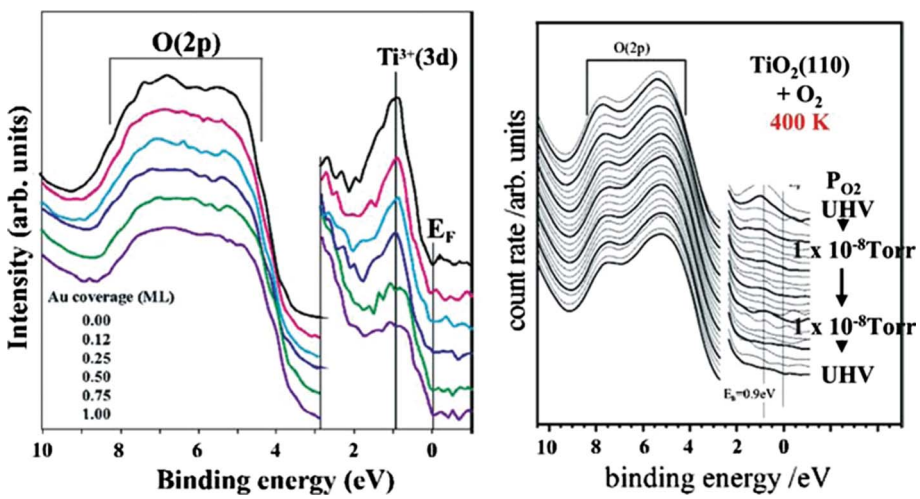

Fig. 13 UPS spectra for a reduced TiO_2 (110) surface with varying degrees of Au coverage at room temperature and UPS spectra for a reduced TiO_2 (110) surface after exposure to O_2 at varying pressures. Taken from ref. 84.

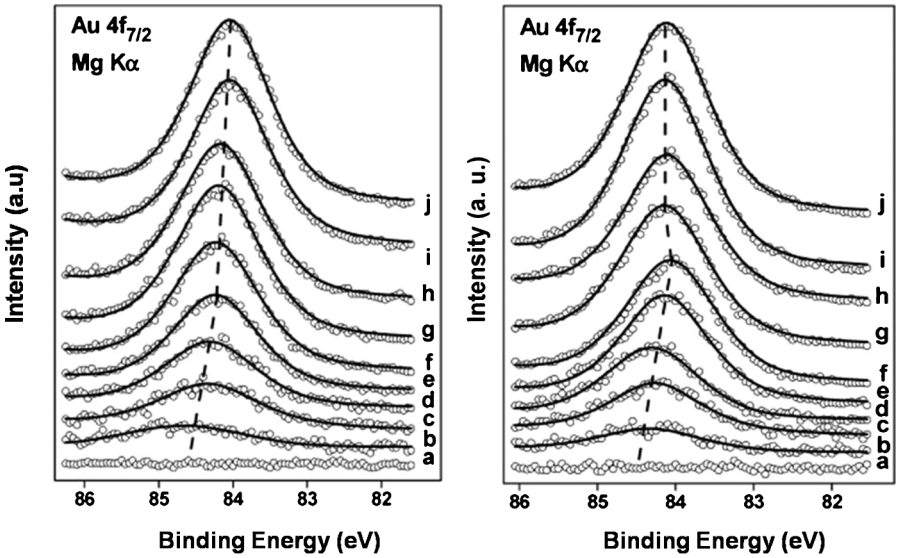

Fig. 14 Au 4f XPS for Au deposition on the stoichiometric (left) and reduced (right) TiO_2 (110) surface. Thickness of Au deposited is (a) 0, (b) 0.125, (c) 0.25, (d) 0.50, (e) 1.0, (f) 1.5, (g) 2.0, (h) 3.0, (i) 5.0, and (j) 10.0 Å. Taken from ref. 87.

downward shift of the core level binding energy was observed for Au thickness coverage of up to 1.5 Å after which the binding energy shifts upwards. The downward shift observed for the reduced surface can be linked to a combination of both particle size effects and charge transfer from O_v defects to the Au clusters. This charge transfer creates negatively charged Au clusters, which along with particle size effects, contributes to a decrease in their core level binding energy. Due to limited defect availability on the reduced surface charge transfer diminishes with increased Au deposition until no charge transfer occurs resulting in the relative upward shift of the core level binding energy. These results are in contrast to another more recent one using elevated-pressure reaction conditions over Au/TiO_2 (110) rutile surface, ambient-pressure X-ray photoelectron spectroscopy (APXPS).[88] The authors found that while the Ti2p and O1s peaks shifted to lower binding energy (by up to 0.5 eV) when compared to UHV conditions, upon exposure of the surface to O_2 (up to 1 Torr), the Au 4f did not shift. The authors attributed the shift of the Ti2p and O1s to band bending of the support (TiO_2).[88] To date there are no reported experiments that have investigated by core level spectroscopy the effect of charge transfer from the support to the metal under photo-excited conditions.

2.5 Surface reactions

Two main concepts are associated with surface catalysis on reducible metal oxides: acid–base reactions and redox reactions. Acid–base reactions arise due to the alternation of charge within metal oxides, and redox reactions occur when the electronic configuration of the surface is altered due to the introduction of defects.[89] Both processes are fundamentally different in their mechanisms, however both processes can be interrelated.

On the TiO_2 surface, Ti cations and O anions are described as Lewis acid and Lewis base sites, respectively, with high electron density molecules (Lewis bases) adsorbing at cation sites and electron accepting molecules (Lewis acids) reacting at anion sites.[89] TiO_2 is predominantly acidic, however, altering the level of surface reduction results in the modification of surface cation acidity and anion basicity. For a reducible oxide surface such as TiO_2, excess electrons associated with defect states reduce surface cations and therefore decrease surface acidity at these cation sites. For both acid–base and redox reactions the adsorption of one reactant onto one surface site will result in molecular or non-dissociative adsorption or alternatively may involve more complex interface reactions that involve the breaking of reactant bonds to produce an adsorbed reactant on two or more surface sites namely dissociative adsorption.[90]

Acid–base reactions occur when there has been electron transfer between the adsorbate and the catalyst surface. An important aspect of acid–base surface reactions is the protonation of surface oxygen which regularly occurs during the dissociation of water molecules. This is typically observed at defect sites such as at O_v defects, where dissociated water transfers a proton to a surface oxygen atom thereby producing two hydroxyl groups and rendering the surface O less nucleophilic.[60,91] In all acid–base reactions the formal oxidation state of all the atoms remains unaltered.

2.5.1 Adsorption and desorption pathways. The capability of individual surface sites to bond with the adsorbate is dependent upon the symmetry, energy and nature of the electronic states located at these surface sites.[46] Adsorption is an exothermic process and only occurs when the attractive interaction between an adsorbate and catalyst surface is stronger than the disordering effect caused by thermal motion. Two main types of adsorption are observed to occur on the catalyst surface: physisorption and chemisorption. Physisorption, or physical adsorption, is defined by the interactive van der Waal's forces between the adsorbate and surface molecules or ions resulting in weak adsorption. Physisorption bonds are typically characterised by adsorption energies <50 kJ mol^{-1} and are easily reversed. Physisorbed adsorbates can undergo diffusion on the catalyst surface and are generally not bound to any specific site.[92,93] Chemisorption, or chemical adsorption, occurs when the

MOs of the adsorbate overlap with those of the surface atoms allowing for the creation of chemical bonding *via* electron sharing. The formation of chemisorbed bonds usually only occurs when an activation barrier has been overcome. This bonding results in the creation of a surface complex which is characterised by adsorption energies >50 kJ mol^{-1} and therefore has stronger adsorption onto the catalyst surface and are consequently more difficult to reverse.[92,93] Usually also observed with chemisorption is the weakening of the adsorbate intramolecular bonds which results in dissociation of chemisorbed molecules.

As well as the metal oxide surface structure being important in determining adsorption mechanics, the alcohol reactant structure is also significant in determining the selectivity of alcohol decomposition.[94] The chemical interaction of ethanol with other solids is largely associated with the presence of the hydroxyl group which has the effect of making ethanol molecules slightly basic.[95] The level of acidity of any given alcohol, and therefore its adsorption mechanics, is known to be dependent on both its polarisability as well as its inductive effects. In the gaseous phase, the inductive effect created by the electron-releasing capability of the alkyl (–CH_3) group is reduced and therefore ethanol is less acidic than it would be in solution. Polarisability is negligible in solution, however in the gas phase it may become more important as the negative charge on the oxygen is not dispersed as it is in solution. These opposing polarisability and inductive effects will influence the adsorption mechanics of ethanol molecules on the TiO_2 surface.[96]

There has so far been no research conducted into the photo-production of hydrogen from ethanol over the rutile single crystal surfaces. However work has been conducted on the general photoreaction/oxidation of ethanol over the single crystal rutile (110) surface as well as more extensive research into the reactions of acetic acid, acetaldehyde, acetone and carboxylic acids, as well as for smaller molecules such as H_2O, O_2, H_2 and CO, over this surface. We will review some of the reactions over TiO_2 single crystal surface before focusing on hydrogen production over real catalysts.

2.6 Simple molecule reactions over rutile TiO_2 (110) surfaces

2.6.1 H_2O on TiO_2. The adsorption mode of H_2O over the rutile (110) surface at room temperature (RT) and below have been studied experimentally using UPS,[97] TPD,[98,99] XPS[98] and DFT.[100] At 160 K the adsorption model proposed for H_2O is molecular at Ti_{5c} sites on the oxidised surface, as well as at O_v defects on the reduced surface. Dissociation of the water molecule can then occur in both cases by a proton binding to a neighbouring oxygen atom. Heating to 200 K results in the majority of the molecularly adsorbed water desorbing and by 320 K most OH species have also been desorbed from the surface.[97] Using DFT calculations, Lindan *et al.*[100] have produced adsorption energies that are compatible with these experimental results and are consistent with a mixed state in which molecular and dissociated water occurred at monolayer (ML) coverage. The adsorption energies were, however, very close for the fully dissociated water (0.99 eV) and the mixed state (1.01 eV) and the difference with the molecular adsorption is still very small (0.91 eV). Therefore water appears to be adsorbed molecularly on defect-free TiO_2(110) rutile surface.

2.6.2 O_2 on TiO_2. Exposing a reduced rutile surface to O_2 results in the quenching of O_v sites on the surface, therefore creating a more oxidised surface. On the rutile (110) surface at 28 K, O_2 is molecularly adsorbed at O_v sites with O_2 coverage dependent upon the number of available surface O_v defects.[101] Upon annealing the molecularly adsorbed O_2 then undergoes dissociation. Epling *et al.* postulated four mechanisms for the dissociative adsorption of O_2 at O_v sites: O_2 dissociation and the filling of two O_v defects, the filling of a single O_v with the second O atom either diffusing into the bulk or being released into the gas phase or the filling of a single O_v with the second atom remaining on the surface as an adatom. TPD results from the rutile surface exposed to water and ammonia showed an increase in the desorption temperatures for these reactants on the pre-oxidised surface as compared to the reduced surface. In order to influence surface reactions in this way Epling *et al.* deduced that O_2 dissociation at an O_v must be accompanied by the binding of the second atom at another surface site, most likely a Ti_{5c} atom. This view, however, does not consider the effect of electronic structure on the adsorption process. For example, Pauli repulsion can be behind destabilisation of NH_3 adsorbed on oxygen-defected surface or may even prevent it from adsorbing on these sites. The presence of surface O adatoms is currently the most widely accepted view as based on numerous STM studies that have identified spots on the Ti_{5c}^{4+} sites upon healing of the O_v defects.[102]

2.6.3 H_2 on TiO_2. Adsorption of H_2 on the rutile (110) surface has only been found to occur at O_v sites which act as electron donors and create H^+ surface ions.[48] On the defect-free surface H_2 adsorption is not observed due to the high activation energy required for breaking hydrogen bonding and the absence of the electronic charge transfer afforded by the presence of O_v defects. Early work by Göpel *et al.*,[103] has indicated that at 300 K dissociative adsorption of H_2 occurred at the O_v-associated Ti_{5c}^{3+} sites. Ionic titanium hydride bonds are formed with H_2 dissociation occurring due to the transfer of two electrons from the O_v. Surface coverage for H_2 adsorption has been found to be low on the rutile (110) surface with a maximum fractional coverage of 0.005 ML indicating that only minimal amounts of H_2 can be adsorbed onto this surface.[99]

2.6.4 CO and CO_2 over TiO_2. CO molecules have weak binding onto Ti cations on the defect-free rutile (110) surface, however the presence of O_v sites on this surface greatly enhances adsorption.[48] This enhanced adsorption is due to the occurrence of electron back-donation from O_v-associated Ti^{3+} ions into the π^* orbitals of the CO molecule.[46] Using TPD, Raupp *et al.*[104] found that CO dosed onto the surface at 150 K molecularly desorbed at around 200 K. At temperatures between 300 and 370 K, Göpel *et al.*[103] observed more strongly bound molecular CO adsorption which upon annealing yielded a small amount of desorbed CO_2 due to the removal of surface O atoms, effectively reducing the rutile surface. On nearly defect-free TiO_2(110) surface physisorption of CO was studied using beam reflection and temperature programmed desorption techniques. A sticking coefficient of about 0.75 was found independent of coverage suggesting that adsorption occurs *via* a precursor-mediated mechanism. At low coverage (0 to 0.5 CO/Ti^{4+}), CO molecules bind through the C to fivefold-coordinated Ti^{4+} cations. The

adsorption occurs preferentially on the Ti^{4+} sites that do not have neighbouring adsorbates. This arrangement minimizes the repulsive interactions between the adsorbed molecules along Ti^{4+} rows. At higher CO coverage (>0.5 ML), the nearest-neighbour Ti^{4+} sites become occupied. The close proximity of the adsorbates results in strong repulsion thus giving rise to a significant shift of the TPD leading edge with increasing coverage. The repulsive adsorbate-adsorbate interactions are most likely due to alignment of CO dipole moments.[105] Göpel *et al.* further reported that CO_2 weakly adsorbed to the rutile (110) surface with adsorption uninfluenced by surface defect density. Due to this, CO_2 desorption has commonly been used as a probe for measuring the extent of surface defect coverage on the rutile (110) surface.[106]

2.6.5 Photoreaction of O_2 over TiO_2. The photoreaction of O_2 on the surfaces of TiO_2(110) rutile single crystal deserves a particular attention because of its fundamental nature that motivated considerable studies, in particular by Yates *et al.* for over a decade.[107–111]

The first thing to consider is that O_2 molecularly adsorbs on surface O defects that are charged with electrons. Upon adsorption, the O_2 molecule becomes negatively charged (O_2^-(a)). Yates and co-workers summarised the process that occur upon UV excitation of O_2-adsorbed TiO_2 surface as follows:[108]

$$h\nu + TiO_2 \rightarrow e + h\ [k_1 F_{h\nu}] \quad (2)$$

$$h + T \rightarrow \text{(hole capture)}\ [k_2] \quad (3)$$

$$e + h \rightarrow \text{(heat or luminescence on recombination sites)}\ [k_3]$$

$$h + O_2^- \rightarrow O_2(g)\ [k_4] \quad (4)$$

where e and h are generated electrons and holes upon UV excitation, T is a hole trap, g is gas phase and the rate constants k_1 to k_4 are given in brackets.

The rate of desorption of O_2 in the gas phase, using the steady state approximation, is therefore expressed by the following equation:

$$\frac{d[\theta_{O_2}]}{dt} = -k_4 \left(\frac{k_1}{k_3}\right)^{1/2} F_{h\nu}^{1/2} [\theta_{O_2}] \quad (5)$$

The equation comes from the rate of [h], d[h]/dt, is equal to $k_1 F_{hv} - k_3$[h][e] = 0; neglecting step (2). Therefore the concentration of holes [h] is:from which eqn (5) is obtained.

$$[h] = \left(\frac{k_1}{k_3}\right)^{1/2} F_{h\nu}^{1/2} \quad (6)$$

Because k_1 and k_3 are intrinsic to TiO_2 (at sufficiently high photon flux) they can be considered constant, and therefore monitoring the rate of desorption as a function of O_2 coverage may be used to obtain k_2. The interesting point is that the calculated rate constant was found to vary by a factor of 100 or more as the chemisorbed O_2 is photo-desorbed. Yates and co-workers interpreted this as due to a fractal kinetic process made by hole neutralisation by percolating electrons present at O-vacancy defects (which do not contain O_2^-(a)).

The main idea is that, as the coverage of adsorbed oxygen decreases, the surface density of the overlapping filled electronic states at vacancy sites increases; this in turn results in decreasing the rate coefficient for O_2 photo-desorption with time.

In another very interesting work Yates *et al.* studied the effect of UV excitation on the photo-desorption of O_2 and compared it to the same reaction upon electron excitation (Fig. 15).[107] The authors determined the kinetics of electron-hole recombination by monitoring the desorption of molecular O_2 from the rutile TiO_2 (110) surface induced firstly by an electron flux and secondly by a photon flux. Under conditions of constant O_2 coverage, the rate of desorption as seen above is dependent on the relationship between hole concentration and the incident electron or photon flux. The plots derived from the photo-desorption of O_2 as observed in Fig. 16 show that electron stimulated desorption (ESD) and photon stimulated desorption (PSD) have differing kinetic orders. In Fig. 16a electron-stimulated O_2 desorption is proportional to the first power of the electron flux indicating that hole depletion has first-order recombination kinetics.[107] In Fig. 16b the photon flux results in 2 branches of desorption both of which adhere to a second order rate law as they show a linear function of the square root of the photon flux ($F_{h\nu}^{1/2}$).[108]

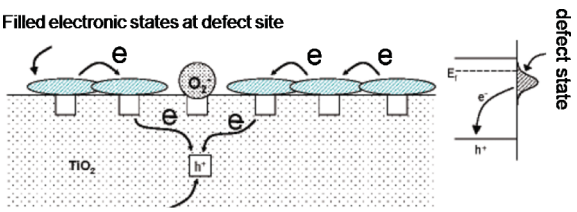

Fig. 15 Schematic diagram showing the electron transport postulated to occur through the extended filled electronic states surrounding O-vacancy sites. From ref. 109.

To understand this we need to invoke again the above equations (2) to (6) but add to them a fifth one related to electron trapping:

$$e + T^+ \rightarrow T\ (k_e) \quad (7)$$

where T^+ is an electron trap center and k_e is the associated rate constant for the reaction.

Now in the case of electron excitation and using the steady state approximation, $d[h]/dt = k_1 F_e - k_2[h][T] = 0$, where in this case F_e (electron flux) has substituted for F_{hv} from which [h] = $k_1 F_e k_2$[T] is obtained. Therefore the overall rate of O_2 desorption is:

$$\frac{d[\theta_{O_2}]}{dt} = -k_4 \left(\frac{k_1}{k_2}\right)^{1/2} \frac{F_e}{T} [\theta_{O_2}] \quad (8)$$

Considering that the hole trap concentration [T] is constant, then [h] is proportional to the electron flux.

The difference in reaction order observed for the two experiments is due to the difference in absorption length of the incident electrons and photons. The electron flux of 100 eV has an electron inelastic mean free path of ~5.6 Å whilst UV light with an energy of 3.4 eV has an absorption length of ~103 Å. Electrons are therefore absorbed in the near surface where there are a larger number of defects and charge trapping sites when

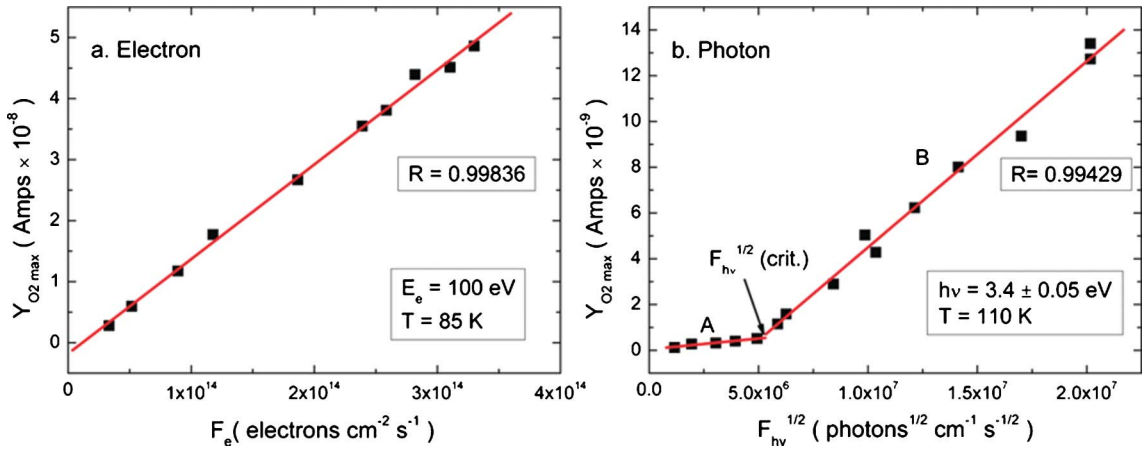

Fig. 16 Plots of O_2 photodesorption over the rutile (110) surface as a function of (a) incident electron flux (F_e) and (b) the square root of the incident UV photon flux ($F_{hv}^{1/2}$). Taken from ref. 107.

compared with the bulk whilst photons will penetrate more deeply.[107] Electron-hole recombination in the near-surface is most likely to be due to Shockley-Read-Hall (SRH) mechanisms whereby electrons or holes are trapped within trapping sites in the band gap formed due to the non-degeneracy of the semiconductor.[109] SRH recombination mechanisms are typically of first order as observed for electron-stimulated O_2 desorption. For photon-induced desorption the longer absorption length indicates that PSD is governed by deeper CB to VB electron-hole recombination mechanisms which are characteristically of second order as observed for the photon-stimulated O_2 desorption.[107]

Along with suitable electron-hole dynamics and the availability of trapping sites for photo-excited charge, any photoreaction also requires the transfer of this charge to the adsorbate.[107] Successful charge separation and subsequent migration of electrons and holes to the semiconductor surface can either reduce or oxidise surface adsorbates. These reduction/oxidation reactions are dependent upon the redox potential of the adsorbate on the catalyst surface relative to the VB and CB. The energy level of the CB minimum represents the photoelectron reduction potential, whilst the top energy level of the VB represents the oxidation potential of the photo-holes. Thermodynamic requirements demand that for the surface photoreaction to commence the base of the CB needs to be more negative than the redox potential of the acceptor species, whilst the top of the VB needs to be more positive than the redox potential of the acceptor species (Fig. 17).

When all conditions are favourable and recombination is avoided, photon-induced excitation of an electron from the VB into the CB can result in further charge migration to adsorbates at the semiconductor surface interface.

2.7 Ethanol reaction behaviour over TiO_2

Barteau stated early on that the general behaviour of alcohols is that of immediate dissociative adsorption on metal oxides. This leads to the formation of an alkoxide bonded to the surface cation with the corresponding proton bound to a surface anion (oxygen) as is typical of acid–base chemistry.[60] This expected principal interaction occurs between the adsorbate and the

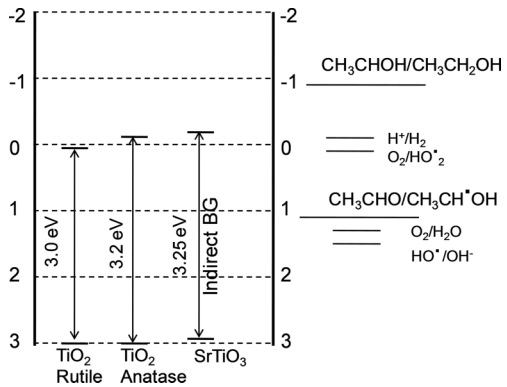

Fig. 17 VB and CB positions of several selected semiconductors with selected redox couple potentials at pH 0.

surface at the O2p levels and the empty states of the Ti3d levels of TiO_2 resulting in the formation of these stable alkoxide species.[112] In the case of ethanol adsorption over TiO_2, this de-protonation would produce ethoxide ($CH_3CH_2O^-$) species bonded to Ti cations and a hydrogen ion bonded to the O^- anion as shown by eqn (2).

$$C_2H_5OH(g) + \mathbf{Ti}(s)\text{–}\mathbf{O}(s) \rightarrow CH_3CH_2O\text{–}\mathbf{Ti}(ad) + H\text{–}\mathbf{O}(ad) \quad (9)$$

where (g) is gas, (ad) is adsorbed and (s) is the surface.

The deprotonation of ethanol on the rutile (110) surface has been shown experimentally by many workers including Jayaweera *et al.*[112] In this work it was found that adsorption of ethanol over TiO_2 is dissociative and has a surface saturation of around 0.5 ML with respect to surface Ti atoms. The coverage was estimated from the attenuation of the XPS O1s and Ti2p peaks of surface caused by screening of surface O and Ti atoms due to adsorption. It is proposed that due to the length of the CH_3CH_2– of ethoxides, two neighbouring ethoxide species will undergo repulsion effectively leaving every alternate Ti cation site free.

Following the formation of stable ethoxide species on the rutile (110) surface, Jayaweera *et al.* found that with increased UV exposure time in the presence of O_2 in the gas phase a decrease in the XPS peak areas of the C1s ethoxide species was observed as well as the introduction of a new peak attributed

to RCOO– species. These changes have been explained by the formation of reactive oxygen radicals on the TiO_2 surface due to the transfer of photoexcited electrons from the TiO_2 VB to the CB, as shown in eqn (10) and (11). The further reaction of O_2^- with ethoxide species may then produce acetaldehyde and acetate as shown in eqn (12):

$$TiO_2 + UV \rightarrow e^- + h^+ \quad (10)$$

$$e^- + O_2(g) \rightarrow O_2^-(ad) \quad (11)$$

$$O_2^-(ad) + CH_3CH_2O(ad) \rightarrow HO_2(ad) + CH_3{-}CHO^{\bullet}(ad) \rightarrow + O(ad) \text{ or } O_2(g) \rightarrow CH_3COO(ad) \rightarrow\rightarrow CO_2(g) + H_2O(g) \quad (12)$$

$\rightarrow\rightarrow$ denotes unidentified intermediate reaction step(s).[108]

Generally on single crystal metal oxide surfaces alkoxide intermediates can either recombine with the dissociated proton to reform alcohol molecules, upon heating, which may then desorb, or can decompose by either dehydrogenation to produce aldehydes or by dehydration to produce alkenes. The dehydration route is favoured on reducible surfaces such as TiO_2 due to the abstraction of oxygen atoms from surface ethoxides by surface O_v sites. A reduced surface therefore encourages selectivity towards dehydration products.[60]

The dehydration of ethanol to form ethylene was early on shown in a work by Gamble *et al.*[113] Ethanol and deuterated ethanol were dosed onto the TiO_2 rutile (110) single crystal surface and subsequent desorption measured using TPD. The TPD data showed desorption peaks for ethanol and ethylene at 650 K in an approximately 1 : 1 ratio. This suggests that the adsorbed ethoxide groups underwent β-hydride elimination with subsequent breaking of the carbon–oxygen bond and release of ethylene gas as shown in eqn (13). More recent work was conducted by Nadeem *et al.* on the same surface.[114] The authors observed acetaldehyde in addition to ethylene in line with previous work on other TiO_2 rutile surfaces. Because ethylene is formed due to ethanol/ethoxide adsorption on oxygen vacancies, its yield is largely dependent on the history of the surface and the number of these oxygen vacancies prior and during the TPD.

$$CH_3CH_2O{-}Ti\ (ad) \rightarrow C_2H_4(g) + H{-}O(ad) \quad (13)$$

$$CH_3CH_2O{-}Ti\ (ad) + H{-}O(ad) \rightarrow C_2H_5OH(g) + O(s) \quad (14)$$

In the same work Nadeem *et al.* conducted UV experiments similar to those conducted by Jayawera *et al.*,[108] but this time using on-line mass spectrometry rather than XPS. The authors found that upon UV excitation in the presence gas-phase oxygen molecules acetaldehyde desorbs (Fig. 18). The same authors also found that the amount desorbed has a square root dependency on O_2 pressure and this was interpreted as due to surface saturation by O_2 molecules at high pressures in a Langmuir-type behaviour.

2.8 Acetone reaction behaviour over TiO_2

The photochemical mechanisms of acetone are of great interest to researchers due to acetone being a common organic reactant, intermediate or product as well as an air-borne contaminant.

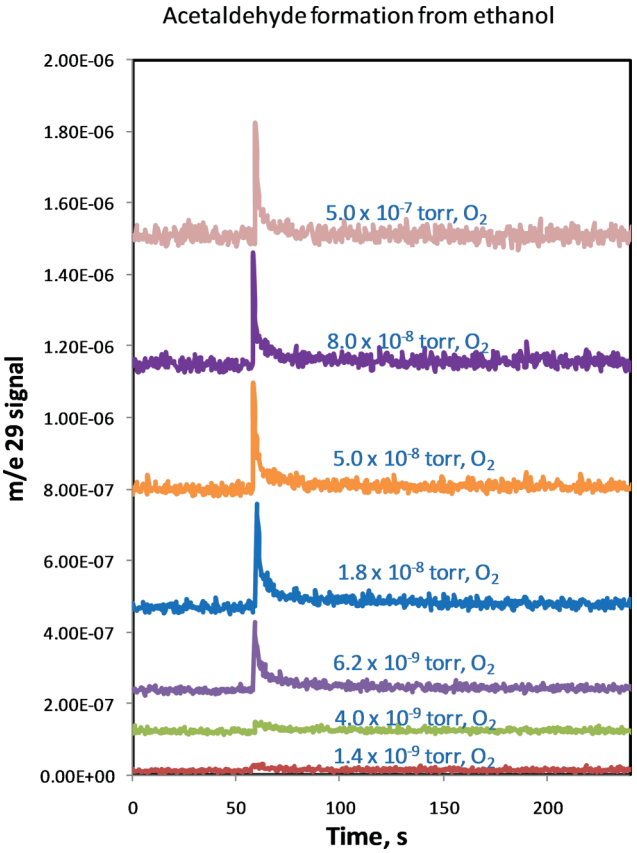

Fig. 18 Acetaldehyde desorption as a function of time upon UV excitation (360 nm) over a rutile TiO_2(110) surface pre-saturated with ethanol at 300 K. The same experiment was repeated at different O_2 pressures as indicated on each spectrum. The surface was cleaned between each experiment. Adapted from ref. 115.

Henderson[115] used TPD and HREELS to determine acetone adsorption and desorption processes on the reduced and oxidised rutile TiO_2 (110) surface. TPD analysis for the reduced surface showed a coverage dependence for desorption with a downward shift in the leading edge of the d_6-acetone desorption spectra with increased coverage indicating destabilisation of acetone–Ti^{4+} sites due to intermolecular acetone repulsions. For the oxidised surface the TPD data showed a first-order desorption peak. Henderson found no evidence that suggested that O_v sites are the binding sites for acetone adsorption or that they were sites that lead to greater binding of acetone to the surface. He suggests that the reason O_v sites are not preferential sites for acetone stabilisation is due to the π* acceptor orbitals of acetone being too high in energy to overlap with the electronic levels of the O_v sites. HREELS revealed that acetone was molecularly adsorbed, as shown in Fig. 19 (left), in a η^1 coordination to Ti^{4+} sites. Based on the C–O stretching frequency measured by

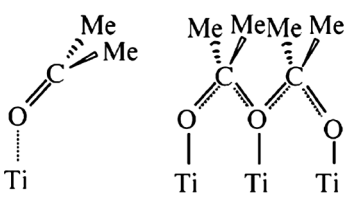

Fig. 19 (left) η^1 acetone, (right) poly-acetone. Taken from ref. 118.

HREELS, which is consistent with a C–O bond somewhere between a single and a double bond, Henderson suggested a poly-acetone surface species is formed, as shown in Fig. 19 (right), whereby molecularly or dissociatively co-adsorbed oxygen attacks the carbonyl carbon of an adjacent molecularly adsorbed acetone resulting in the rehybridisation of the carbonyl π system.

Further work by Henderson[116] using TPD on the effects of co-adsorption of water with acetone shows that on the reduced surface increased water coverage following acetone adsorption lead to an increase in the amount and degree of surface acetone destabilisation. An exponential fit of this data is shown in Fig. 20 comparing the fraction of d_6-acetone desorption from both the reduced and oxidised surfaces.

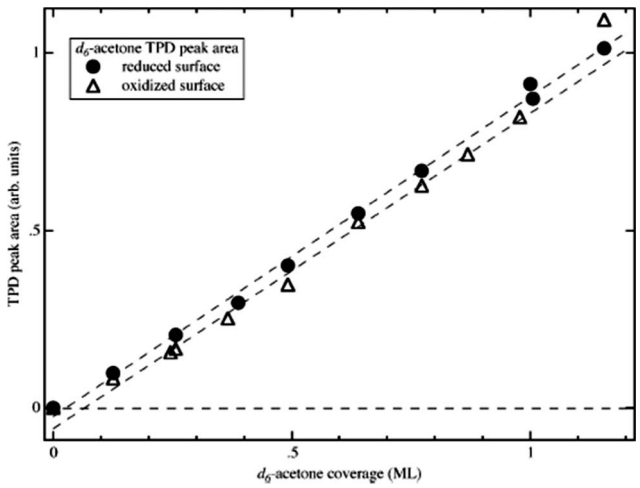

Fig. 20 Exponential fit of TPD peak area data from mass 46 showing the fraction of d_6-acetone desorbing above 275 K (above the water layer TPD feature) as a function of water coverage. Taken from ref. 116.

Henderson suggests that acetone on the pre-oxidised surface has greater resistance against water displacement due to the acetone–oxygen complex formed from reactive surface oxygen species which has greater stability than the molecularly adsorbed acetone species observed on the reduced surface.

Further work by Henderson[117] uses post-irradiation TPD to show the photodesorption products of acetone on the rutile (110) surface. The TPD spectra in Fig. 18 reveals thermally activated decomposition (>175 K) of acetone on the surface that with increased UV exposure produced acetate groups on the surface which then undergo desorption as ketene at around 620 K. The inset in Fig. 21 shows changes in surface coverage of acetone and ketene with increased UV exposure. The acetone coverage can be taken as an absolute coverage and the exponential decay of acetone can therefore be described as a first-order process. The ketene curve cannot be taken as absolute coverage, but the increase of this curve as that for acetate decays indicates that ketene is the only detectable C-containing product of acetone following UV irradiated TPD.

Photodesorption experiments using d_0-acetone on the rutile (110) surface showed that upon UV irradiation a strong spike in the signal occurred for mass 15, as well as lesser spikes for masses 13 and 14. The ratio of these three peaks was consistent with the gas phase spectrum of methyl radicals. This experiment

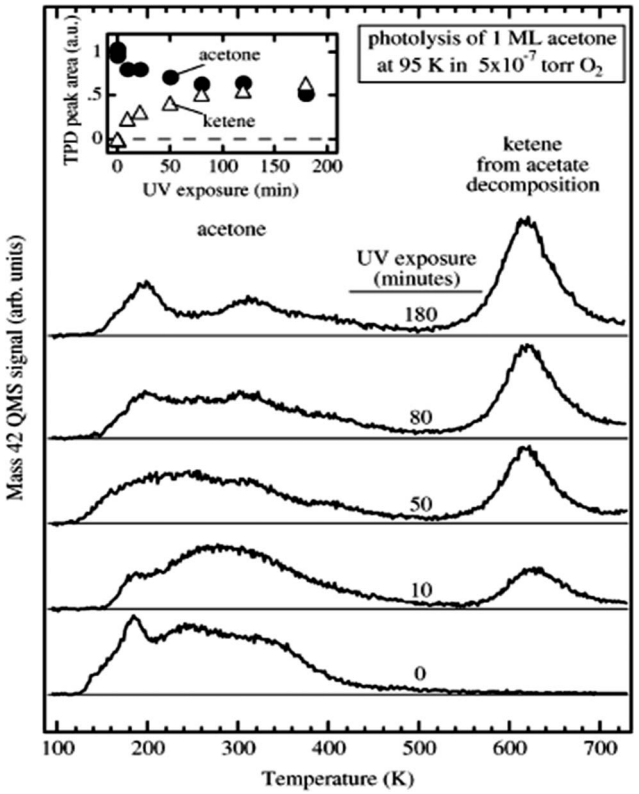

Fig. 21 TPD spectra of mass 42 for 1 ML surface coverage of acetone on rutile (110) at 95 K irradiated with UV light for varying lengths of time in 5×10^{-7} Torr O_2. Inset shows TPD peak area data for acetone and ketene as a function of UV exposure. Taken from ref. 117.

was repeated using d_6-acetone as the adsorbate which showed a spike in the signal upon UV irradiation for mass 18 but not mass 20. This further indicates that the photo-desorbed products produced from the cleaving of the C–C bond were methyl radicals rather than methane. From data obtained before and after photo-desorption experiments of methyl radical ejection a plot of the photo-oxidation cross-section of acetone was obtained, as shown in Fig. 22, where a faster initial acetone photo-oxidation rate was followed by a second slower rate.

Henderson suggests that the observed methyl radical ejection requires the formation of poly-acetone, as shown in Fig. 19, through the interaction of adsorbed acetone and co-adsorbed oxygen molecules or atoms, as shown in eqn (15). The fast acetone photo-oxidation rate is then represented by eqn (16):

$$\eta^1\text{-acetone(ad)} + O/O_2\text{(ad)} \rightarrow \text{poly-acetone(ad)} \quad (15)$$

$$\text{Fast: poly-acetone(ad)} + UV \rightarrow \text{acetate(ad)} + CH_3\text{(g)} \quad (16)$$

Since the initial photo-oxidation rate in the first few seconds of UV excitation was over 2 orders of magnitude faster than later on, it can be assumed that the slower photo-oxidation rate is not limited by the flux of electron-hole pairs to the surface as photon flux remained constant over the period of UV exposure. An exception to this would be if the poly-acetone complex was directly excited by UV light during the initial fast rate followed by some TiO_2-mediated excitation during the second slower rate. It is presumed for the slower photooxidation rate that the rutile surface's ability to regenerate the poly-acetone species is the

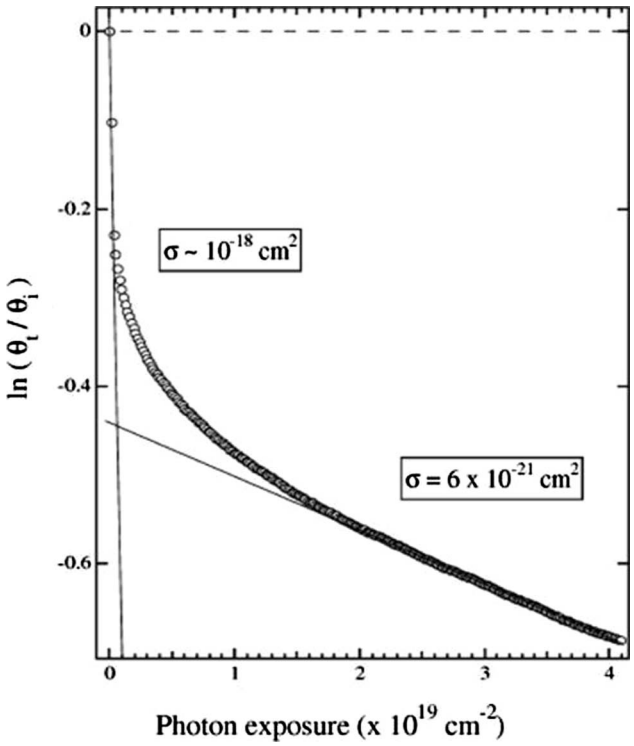

Fig. 22 Acetone photo-oxidation cross section plot obtained from methyl radical photo-desorption trace. Taken from ref. 117.

mechanism that limits this rate. This process is determined by eqn (17) to (20):

$$\text{Slow: } TiO_2 + UV \rightarrow e^-/h^+ \text{ pairs} \quad (17)$$

$$Ti^{4+} + e^- \rightarrow Ti^{3+} \quad (18)$$

$$O_2(g) + Ti^{3+} \rightarrow O_2^-(ad) + Ti^{4+} \quad (19)$$

$$O_2^-(ad) + \eta^1\text{-acetone(ad)} \rightarrow\rightarrow \text{poly-acetone(ad)} \quad (20)$$

From eqn (10) to (13) it can be seen that the slower rate depends upon the rutile ability to generate electron-hole pairs under UV excitation; transport and trapping of excited electrons at surface Ti^{3+} sites; subsequent access of O_2 to Ti^{3+} sites and finally the regeneration of the poly-acetone species.

2.9 Acetaldehyde reaction behaviour over TiO_2 (110) surface

Zehr and Henderson[118] have conducted Photo Stimulated Desorption (PSD) and TPD over the rutile TiO_2 (110) single crystal surface to investigate the thermal and UV-induced surface reactions of acetaldehyde. TPD analysis of both the reduced and pre-oxidised surfaces showed, when both surfaces were exposed to gaseous O_2, some acetaldehyde decomposition occurred, caused by a reaction involving oxygen, and resulted in the formation of surface acetates. On the oxidised surface the acetates were further seen to thermally decompose to form ketene which desorbed from the surface at *ca.* 700 K. The oxidation of acetaldehyde to acetate has a low enough activation barrier so as to allow this reaction to occur on the RT O_2-dosed rutile (110) surface. The formation of adsorbed acetate accounted for <10% of total acetaldehyde adsorption. PSD on the oxidised surface upon UV exposure showed a large signal for methyl radicals as previously observed in the photo-oxidation of acetone on the rutile (110) surface.[117] Following methyl ejection a C_1 fragment is left upon the surface which after reaction with oxygen makes formate species that decompose at about 550 K. As was observed for methyl ejection from the acetone-saturated surface,[117] the presence of co-adsorbed oxygen as well as a pre-heated surface was required for acetaldehyde photochemistry to occur. As proposed for the acetone-saturated surface, the thermal reaction shown in eqn (21), producing a photoactive acetaldehyde-oxygen complex, is expected to be a precursor for acetaldehyde photo-dissociation upon exposure to UV light (eqn (22)).

$$\eta^1\text{-acetaldehyde(ad)} + O/O_2\text{(ad)} \rightarrow \text{acetaldehyde-oxygen complex(ad)} \quad (21)$$

$$\text{acetaldehyde-oxygen complex(ad)} + UV \rightarrow CH_3(g) + \text{formate(ad)} \quad (22)$$

2.10 Acetic acid reaction behaviour over TiO_2 (110) surface

The general interaction of carboxylic acids over transition metal oxide surfaces at RT is through dissociative adsorption (luminescence, Shen, Philip's work). Guo *et al.*[119] determined a while ago from LEED and ESDIAD patterns of acetic acid dosed onto the rutile TiO_2 (110) surface that dissociation of the O–H bond occurred resulting in ordered acetate and hydroxyl groups, as shown in eqn (23):

$$CH_3COOH(g) + Ti(s)\text{–}O(s) \rightarrow CH_3COO\text{–}Ti(ad) + H\text{–}O(ad) \quad (23)$$

From the observed (2x1) LEED pattern coverage was taken to be 0.5 ML in relation to the surface density of Ti^{4+} ions, with the distance between acetates in the [001] direction being double the unit cell length of the clean rutile surface. Analysis of the signal from the ESDIAD patterns of the (2x1) adsorbate layer indicated that acetates were adsorbed onto the rutile surface with their major molecular axis perpendicular to the surface normal in a bridging form. In a later work by Guo *et al.*,[120] STM images further supported the bridging form for acetate adsorption. The acetates were observed along the [001] direction correlating in position to bright rows on the clean surface. The distance observed between acetates was equal to double the clean rutile surface unit cell length with the distance between acetates along the $[1\bar{1}0]$ direction equal to the corresponding unit cell of the clean surface.

Idriss *et al.*[121] used XPS on the acetic acid-dosed rutile (110) surface in order to compare temperature effects on the surface coverage of acetates both in the presence and absence of O_2 as well as under both dark and UV conditions. Firstly acetic acid was dosed onto the rutile surface at 300 K under dark conditions and the surface temperature increased. Upon heating, a decrease in the number of surface acetates was observed with almost full acetate desorption by 600 K. On exposing the acetate saturated surface to UV light without O_2 exposure there is only a slight decrease observed in the C(1s) peaks that are attributed to $–CH_3$ and COO– groups indicating that neither the rutile surface in-plane nor bridging oxygens are involved in this photoreaction. However in the presence of oxygen UV

exposure produces a noticeable reduction in the C(1s) XPS peaks indicating that the presence of gas-phase oxygen, as either physisorbed oxygen or oxygen atoms adsorbed at O_v sites, is vital for acetate photodecomposition. Idriss *et al.* argue that any O_v sites on the surface will have been healed by acetic acid adsorption and therefore be unavailable for oxygen molecules or ad-atoms to adsorb to. Idriss *et al.* state that it is more likely that oxygen adsorption is photon stimulated with enhanced electron transfer from the rutile CB to surface oxygen molecules creating O_2^- radical species. These radicals then react directly with the adsorbed acetates. Plotting the calculated C(1s) XPS peak areas as a function of UV illumination time in the presence of O_2 shows that the acetate decays linearly. This indicates that the photoreaction cross-section is not sensitive to the initial surface acetate coverage and that adsorption of acetates and O_2 are not in competition for the same adsorption sites.

Further work on the rutile (110) surface conducted by Uetsuka *et al.*[122] used trimethyl acetic acid as the reactant. Upon trimethyl acetic acid adsorption at RT trimethyl acetate (TMA) anions are formed on the surface. Adsorption is observed *via* deprotonation of the trimethyl acetic acid with TMA anions bridging two surface Ti^{4+} atoms and the proton binding to a bridging O^{2-}. The main surface reaction following UV excitation is shown in eqn (24) involving the capture of a hole from the rutile VB and leading to the decomposition of TMA to *tert*-butyl radicals:

$$(CH_3)_3CCOO^-(ad) + h^+ \rightarrow (CH_3)_3C(ad) + CO_2(g) \qquad (24)$$

The *tert*-butyl radicals then subsequently desorb as isobutene. The corresponding electron (to the hole trapped by TMA in eqn (24)) is trapped at a surface Ti causing its reduction from Ti^{4+} to Ti^{3+}. UV photodesorption experiments of the TMA-covered surface revealed that in the absence of O_2 isobutene desorption monotonically decays as a function of irradiation time. Exposure of the surface to O_2 under dark conditions increased isobutene desorption indicating that anaerobic decay of the reactants cannot be attributed to their disappearance on the surface. Consequently Uetsuka *et al.*[122] suggested that the electrons that cause the reduction of Ti^{4+} to Ti^{3+} undergo recombination with holes and therefore cease the reaction in eqn (24). Upon exposure of the surface to O_2 the electrons trapped at Ti^{3+} sites are removed by adsorbed O_2 and therefore become unavailable for recombination, allowing isobutene desorption to continue. From STM images taken in this study it was observed that local TMA coverage could go from zero to saturation within a few lattice units and that the TMA was heterogeneously desorbed across the surface upon UV irradiation. This indicates that recombination of trapped electrons with holes is localised rather than delocalised. Delocalised recombination would be accompanied by a laterally uniform concentration of holes and therefore a more homogeneous coverage of TMA which is not observed. This work by Uetsuka *et al.*[122] indicates that the redox reaction of TMA over the rutile (110) surface is spatially modulated with the photo-oxidation rate of TMA increased when parts of the surface have free sites for O_2 adsorption. Adsorbed O then has the ability to accept electrons from Ti^{3+} which would otherwise be lost to electron-hole recombination and prevent isobutene desorption.

Wilson & Idriss[123] studied the photoreaction of acetic acid over the rutile (001) surface reconstructions {011} and {114}. On these surfaces the same mode of adsorption for acetic acid as previously shown in eqn (23) was observed. Upon UV excitation, steady-state reactions on both the {011} and {114} surface reconstructions resulted in the reaction products of CO_2, CH_4 and ethane (the photo-Kolbe reaction). When no background O_2 pressure is present a spike in ethane desorption was observed with a subsequent decrease over time as shown in Fig. 23. By increasing the O_2 pressure with continued UV illumination the signal for ethane as shown in Fig. 23 was steady. These results indicate that the formation of ethane consumes oxygen from the lattice.

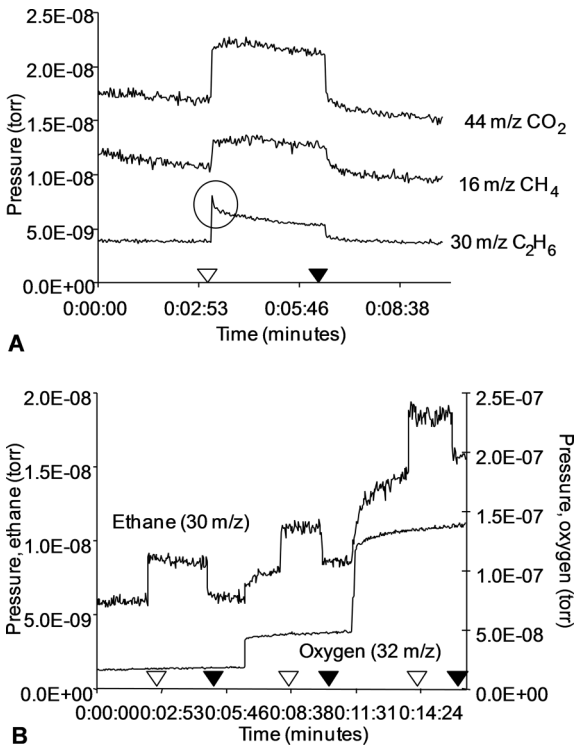

Fig. 23 A. Steady-state acetic acid reaction on the {011} surface reconstruction with open triangle representing UV light on and the closed triangle UV light off. B. Steady-state acetic acid reaction to ethane on the {011} surface reconstruction with increasing O_2 pressure.[123]

Due to both surfaces yielding the same reaction products upon exposure to UV light, the local arrangement of the surface atoms had no effect on reaction product selectivity. However, the {011} surface was found to have a greater reactivity for the formation of ethane than the {114} surface. The different arrangement of surface atoms for the {011} and {114} reconstructions affects the surface reactions occurring due to the differing electronic properties associated with these atomic arrangements such as changing the dielectric constant or surface band gap. The quantum yield of a photoreaction is related to the depletion layer[124] and therefore Wilson *et al.* calculated that the depletion layer in the {011} reconstructed surface is around three times larger than in the {114} reconstruction indicating that photo-induced electrons and holes at the {011} reconstruction will have reduced recombination rates as compared to the {114} reconstruction.

2.11 Photo-production of hydrogen from ethanol on real catalysts

There is a non-negligible amount of work conducted to make hydrogen from ethanol over M/TiO_2 powder using photocatalytic processes.[2,50,114,125–135] Among the factors affecting the reaction is the metal loading,[50,125] with some attempts made to correlate particle size with photoreaction efficiency,[50,131] to the polymorph nature of TiO_2 (anatase *versus* rutile,[50] brookite *versus* anatase,[132] mixed phases[132,135]) as well as to the particle size of the support.[133] Some of these results are presented in more details below.

Nadeem *et al.*[131] recently conducted work comparing the dark and photocatalytic reactions of ethanol over Au particles deposited on TiO_2 anatase nano- (*ca.* 10 nm) and micro- (~0.15 μm) particle catalysts (Fig. 24). The Au particles were of uniform and similar dimension with mean particle sizes of ~5 nm and ~7 nm on the micro- and nano-sized TiO_2 respectively.

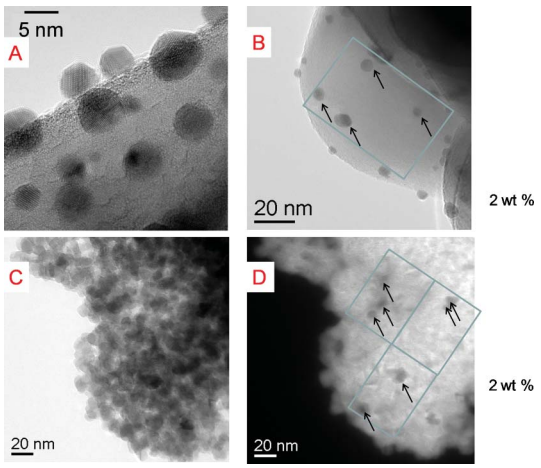

Fig. 24 TEM images of 2 wt% Au/TiO_2 anatase microparticles (A and B) and of 2 wt% Au/TiO_2 nano-particles (C and D). Images A and B show two different areas of the micro-particle catalyst at two different magnifications. Images C and D show the same area of nano-particle catalyst conducted in bright and dark field modes to highlight the presence of Au particles (D). The arrows indicate unambiguous Au particles in images B and D. Note: the rectangles in images B and D are of the same size (45×65 nm^2). From ref. 135.

IR spectra were recorded at 300 K for the modes of adsorbed species as a function of surface temperature under dark conditions, as shown in Fig. 25. As can be seen from Table 1 showing the IR band assignment on 2 wt% Au/TiO_2 anatase nano-particles, as well as those previously reported for pure TiO_2 anatase[136] and CeO_2,[137] there was no noticeable difference between the IR bands observed for 2 wt% Au/TiO_2 and those obtained for TiO_2. This indicated that the mode of ethanol adsorption in the presence of Au is not altered as seen by IR. Also using IR the effect of reaction temperature on the dissociatively adsorbed ethoxide species was monitored. Up to 615 K a steady but small decrease in the number of surface ethoxides was observed with a sharp loss of surface ethoxides subsequently seen after. At 675 K less than 10% of ethoxides were present on the surface which related to the formation of surface carbonates.

Table 1 IR band assignments for ethanol adsorbed on Au/TiO_2 anatase nano-particles with those reported in the literature for adsorption on TiO_2 anatase[132] and CeO_2[133]

Modes	TiO_2 anatase[136]	Au/TiO_2 (this work)	Au/CeO_2[137]
ν O–C/ν C–C (cm^{-1})	1150	1150 (shoulder)	1109
	1100	1120	1065
	1070	1070	1038
		1050	
δ CH_3 (cm^{-1})	1360	1375	1362
ν_s CH_3 (cm^{-1})	2875	2870	2875
ν_a CH_2 (cm^{-1})	2930	2930	2933
ν_a CH_3 (cm^{-1})	2975	2970	2971

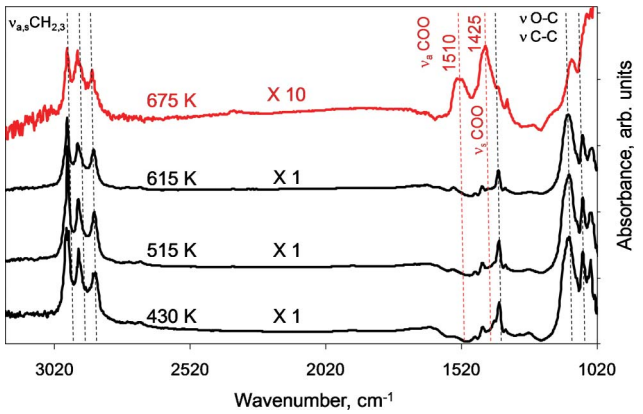

Fig. 25 Effect of temperature on the population of surface ethoxides and other minor reaction intermediates on 2 wt% Au/TiO_2 anatase nano-particles. The surface was first dosed with ethanol at 300 K, then heated to the indicated temperatures under dynamic vacuum for a few seconds and cooled to 300 K to collect the spectra. From ref. 135.

Nadeem *et al.* then performed ethanol TPD on a H_2 reduced catalyst under continuous flow (1 atm) at 673 K, Fig. 26. The product profile gained was dominated by a wide temperature peak for un-reacted ethanol desorption from 370 K to 650 K. Ethanol desorption occurs due to the recombination of

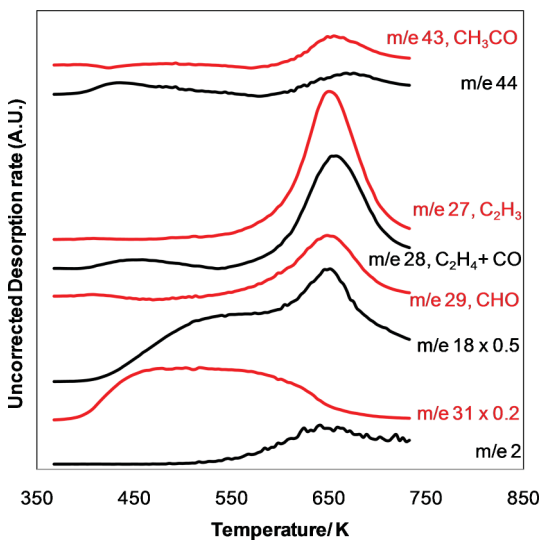

Fig. 26 Temperature programmed desorption after ethanol adsorption at saturation coverage at 300 K on 2 wt% Au/TiO_2 anatase nano-particles. Taken from ref. 135.

Table 2 Surface and bulk properties of 2 wt% Au/TiO_2 anatase nano- and micro-particles

Catalyst	BET ($m^2\ g^{-1}_{catal}$)	XPS Au4f/ Ti2p	Mean Au particle size (nm)	TiO_2 particle size (nm)
Au/TiO_2 (nano-)	105	0.016	*ca.* 7	*ca.* 10
Au/TiO_2 (micro-)	10	0.046	*ca.* 5	*ca.* 150

surface ethoxides with H^+ ions gained from the hydroxyl groups that are formed when ethanol dissociatively adsorbs. However some of these hydroxyl groups will desorb as water molecules. Over the temperature range 650–670 K many products were seen to desorb including acetaldehyde, ethylene, CO, CO_2 and additional water. The ratio of the dehydrogenation reaction from ethanol forming acetaldehyde to the dehydration reaction from ethanol forming ethylene is around 2. Photo-catalytic reactions were also run on both the micro- and nano-anatase monitoring hydrogen production as a function of UV irradiation time, as shown in Fig. 27. Following the induction period the slopes of the lines were roughly equivalent with the nano-sized catalyst, showing hydrogen production around an order of magnitude higher than for the micro-sized catalyst. Following normalisation of the data with respect to surface area both catalysts produces a similar specific reaction rate. From this data it was indicated that the specific reaction rate is independent of the support particle size and that this indicates that the rate of the reaction simply tracks the number of Au NPs on the support. Normalisation of the reaction rate to surface area could mean that electron transfer within the anatase support is unaffected by moving from nano- to micro- (bulk) sized particles (see Table 2 for details on the catalysts). The delocalisation or localisation of electronic wave functions is thought to be an important feature for electron transfer within TiO_2 with the e^-–h^+ recombination rate decreased in localised states. Density Functional Theory (B3LYP) is a computational method known to give acceptable band gap separation in TiO_2. Computations

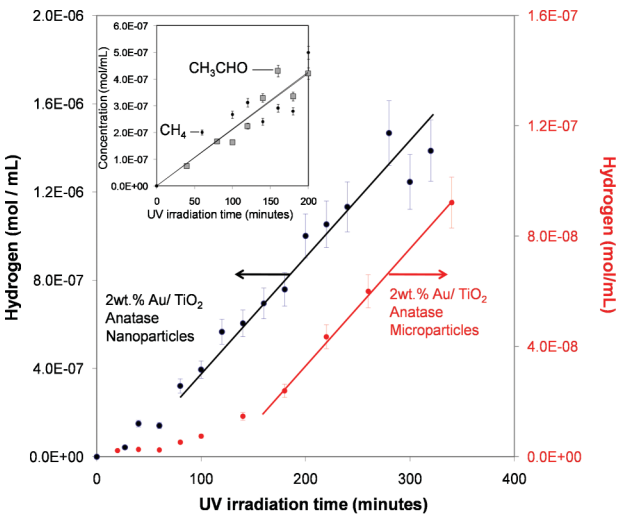

Fig. 27 Hydrogen formation as a function of time during the photocatalytic reaction of ethanol over 2 wt% Au/TiO_2 anatase nanoparticles and 2 wt% Au/TiO_2 anatase micro-particles at 300 K. Catalyst concentration = 6.5 mg/100 mL. Taken from ref. 135.

of the HOMO and LUMO electronic levels of TiO_2 anatase ($Ti_{21}O_{70}H_{54}$) and rutile ($Ti_{23}O_{80}H_{68}$) clusters[138] has shown that the electronic wave functions are delocalised unless electrons are injected directly into the clusters. Furthermore using a similar computational method it was found that local defect states are only seen in the band gap for TiO_2 particles of 1 nm and less.[139] These computational results combined with the experimental results from Nadeem *et al.* indicate that for any marked change to be observed in the electronic properties of TiO_2 NPs they must be of 1 nm or less in size. The other photoreaction products as monitored by TPD showed that the principal reaction is of dehydrogenation of ethanol to acetaldehyde:

$$CH_3CH_2OH \rightarrow CH_3CHO + H_2 \quad (25)$$

However some of the acetaldehyde produced decomposes to CH_4 and CO.

The overall process of the photoreaction of ethanol producing acetaldehyde and hydrogen that is postulated to be occurring is shown in Scheme 1. Firstly irradiation of the surface with UV light lead to the excitation of electrons from the VB to the CB, with a fraction of these electrons in the CB then transferred to Au NPs. H^+ ions may be present at these Au NPs following the de-protonation reaction of ethanol to form ethoxides (eqn (9)) and the reaction of ethoxides forming the de-protonated form of α-hydroxyethyl radicals (reaction 2a, Scheme 1) and acetaldehyde (reaction 2b, Scheme 1). From these two reactions an ethanol molecule will have injected two electrons into the TiO_2 CB. In the case of TiO_2 the time lag between these two electron injections is very fast. If the time lag was slow we may expect to see the radical made in reaction 2a combine to give 2,3-butanediol as has been observed for ZnS NPs,[140] however this compound was not detected for TiO_2. Once acetaldehyde has been formed it was then removed from the surface due to its adsorption energy being smaller than that of ethanol.

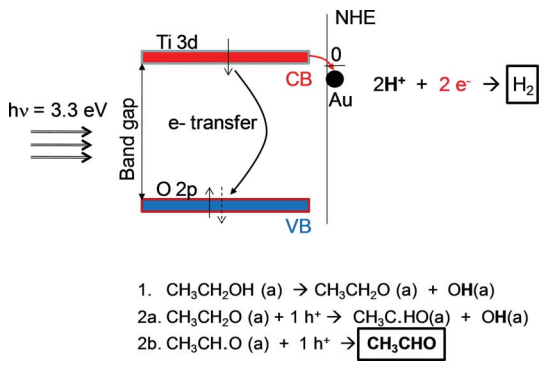

Scheme 1 A representation of the reactions involved in hydrogen production from ethanol over Au/TiO_2 under photo-excitation. The two hydrogen ions formed in reaction (1) and (2a) are reduced by two electrons upon their transfer from the CB to Au particles. Ethoxides inject two electrons into the VB and acetaldehyde is consequently formed. The position of Au particles with respect to the CB is approximate as this varies with the particle size; see ref. 135 for more details.

In a more recent work the same authors[50] have studied the effect of Au particle size deposited on TiO_2 anatase and rutile of the same size. Two main observations are worth mentioning. First the rate for hydrogen production is about two orders of

magnitudes higher on Au deposited on anatase nanoparticles when compared to that on Au particles deposited on rutile nanoparticles. The authors interpreted this as due to the fast electron-hole recombination rate on rutile compared to that on anatase.[50] The second important observation is that Au particle size has no noticeable effect on the reaction rate in the 3 to 12 nm range. The authors did not study the effect of Au particle size smaller than 3 nm though.

It is worth addressing in this last section the combined effect of more than one phase of TiO_2 on the reaction. This effect is commonly known as synergism or the synergistic (or synergic) effect; two substances together have a more pronounced effect on a particular system compared the sum of the effects for each substance separately. This effect has received some attention in the case of TiO_2 when it was realised that Degusa P25 TiO_2 (which is composed of 80% anatase and 20% rutile) is more active for the many photo-excited reactions than the equivalent sum of the anatase and rutile phases. For example, in a work by Zhang *et al.*[141] it was reported that making TiO_2 anatase nano-particles on top of TiO_2 rutile particles resulted in a four times enhancement of the normalised rate per unit area for hydrogen photo-production from water/methanol when compared to TiO_2 anatase alone. The reason for this was invoked as due to the formation of surface junction promoting the spatial charge separation in the surface region. This surface junction would facilitate the transfer of the photo-generated electron from the conduction band of the rutile phase to trapping sites on the anatase surface which results in improvement of the charge separation efficiency and therefore enhances the photo-catalytic activity. In another work by Hurum *et al.*,[142] a study by Electron Paramagnetic Resonance (EPR) was conducted on TiO_2 P25 under photo-illumination. The authors identified an anatase-rutile interface trapping site at the distorted interfacial region at $g = 1.979$. Upon band-gap illumination holes appear at the surface and preferentially recombine with electrons with electrons in surface trapping sites. In other words in the mixed-phase TiO_2, photo-generated holes are trapped exclusively on the particle surface. In another recent paper by other workers the production of hydrogen over Pt/TiO_2 was studied over TiO_2 anatase, brookite and a mixture of both.[132] The authors have found that Pt deposited on TiO_2 brookite has higher activity when compared to Pt deposited on TiO_2 anatase. The authors attribute the difference as due to the higher conduction band level of the brookite structure compared to that of the anatase. The authors also found that when both phases are present the rate of hydrogen production was higher than that observed on a single phase. Equally important the authors observed that the production is sensitive to the surface area in the case of brookite anatase mixture with smaller surface area giving higher activity particularly once normalised to the same unit areas. They interpreted this as due to crystallinity effect.

In a similar work but focusing on the anatase and rutile phase other workers have found that the presence of both phases also had a positive effect on hydrogen production.[134] The authors gave the following explanation (Scheme 2): Because the band gap of the rutile phase is about 0.2 eV smaller than that of the anatase the number of charge carriers is higher. At the interface between the anatase, rutile and Au particles electrons can migrate from one particle to other. An electron initially excited from the valence band to the conduction band in the rutile structure may migrate to the anatase particle and benefits from a far slower electron-hole recombination rate. Therefore the rutile is simply acting as an electron reservoir for the anatase phase at the interface.

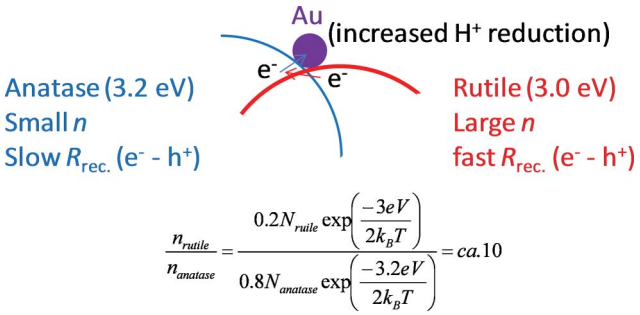

Scheme 2 Postulated explanation for the enhancement of the reaction rate for hydrogen production from ethanol over Au/TiO_2 (anatase + rutile). Au particles at the interface between the anatase and rutile phases will benefit from the higher charge carriers number (n) in rutile and the slower electron-hole recombination rate ($R_{rec}(e^- - h^+)$) in the anatase phase. Taken from ref. 134.

Conclusions

The photoreaction of organic compounds over TiO_2 and noble metal/TiO_2 is rich in many fundamental principles in addition to its important applied aspect for energy generation from renewable systems using renewable sources (such as light from the sun). On model systems the photo-oxidation principles are presented, in particular the role of adsorbed oxygen atoms and surface oxygen defects on the reaction rates. For the photo-production of hydrogen from ethanol the Au/TiO_2 system has shown three interesting non-correlations: the absence of charge transfer for the support to the metal, the absence of particle size effect on the photoreaction up to 12 nm size and the absence of particle size effect of TiO_2 in the 10 to 150 nm size range. On the contrary the presence of the bulk effect is clearly seen with two orders of magnitudes difference in the reaction rate between the anatase and the rutile (for hydrogen production) and a possible synergistic effect between both phases. It is worth mentioning that the complete conversion of ethanol is not achieved and only one third of the hydrogen is extracted with the present knowledge. The challenge will be in designing photo-catalysts for hydrogen production that are capable of breaking the carbon-carbon bond at the operating (ambient) conditions. The reaction mechanism for hydrogen production is presented. Molecular hydrogen is formed *via* electron transfer from the conduction band to the gold particles while a successive two electrons transfer from ethanol to the valence band occurs.

References

1 P. P. Edwards, V. L. Kuznetsov, W. F. David and N. P. Brandon, *Energy Policy*, 2008, **36**, 4356.
2 Y. Z. Yang, C. H. Chang and H. Idriss, *Appl. Catal., B*, 2006, **67**, 217.
3 R. M. Navarro, M. C. Sanchez-Sanchez, M. C. Alvarez-Galvan, F. del Valle and J. L. G. Fierro, *Energy Environ. Sci.*, 2009, **2**, 35.
4 M. Balat, *Int. J. Hydrogen Energy*, 2008, **33**, 4013.

5 G. W. Crabtree, M. S. Dresselhaus and M. V. Buchanan, *Phys. Today*, 2004, **57**, 39.
6 J. N. Armor, *Appl. Catal., A*, 1999, **176**, 159.
7 D. Wang, S. Czernik and E. Chornet, *Energy Fuels*, 1998, **12**, 19.
8 C. Rioche, S. Kulkarni, F. C. Meunier, J. P. Breen and R. Burch, *Appl. Catal., B*, 2005, **61**, 130.
9 A. N. Fatsikostas, D. I. Kondarides and X. E. Verykios, *Chem. Commun.*, 2001, 851.
10 M. Steinberg and H. C. Cheng, *Int. J. Hydrogen Energy*, 1989, **14**, 797.
11 M. Callahan, in *Proceedings of 26th Power Sources Symposium*, Red Bank, N.J., 1974, pp. 181.
12 J. Pohleny, N. Scott, Vol. U.S. Patent No 3 (Ed.: (UOP).), 1966, pp. 284.
13 D. K. Liguras, K. Goundani and X. E. Verykios, *Int. J. Hydrogen Energy*, 2004, **29**, 419.
14 K. Hohn and Y. C. Lin, *ChemSusChem*, 2009, **2**, 927.
15 D. Wang, S. Czernik, D. Montane, M. Mann and E. Chornet, *Ind. Eng. Chem. Res.*, 1997, **36**, 1507.
16 S. Rapagnà, N. Jand and P. U. Foscolo, *Int. J. Hydrogen Energy*, 1998, **23**, 551.
17 S. Turn, C. Kinoshita, Z. Zhang, D. Ishimura and J. Zhou, *Int. J. Hydrogen Energy*, 1998, **23**, 641.
18 Y. Guo, S. Z. Wang, D. H. Xu, Y. M. Gong, H. H. Ma and X. Y. Tang, *Renewable Sustainable Energy Rev.*, 2010, **14**, 334.
19 Y. Calzavara, C. Joussot-Dubien, G. Boissonnet and S. Sarrade, *Energy Convers. Manage.*, 2005, **46**, 615.
20 Y. J. Lu, L. J. Guo, C. M. Ji, X. M. Zhang, X. H. Hao and Q. H. Yan, *Int. J. Hydrogen Energy*, 2006, **31**, 822.
21 X. Xu, Y. Matsumura, J. Stenberg and M. J. Antal, *Ind. Eng. Chem. Res.*, 1996, **35**, 2522.
22 M. J. Antal, S. G. Allen, D. Schulman, X. Xu and R. J. Divilio, *Ind. Eng. Chem. Res.*, 2000, **39**, 4040.
23 D. Wang, S. Czernik and E. Chornet, *Energy Fuels*, 1998, **12**, 19.
24 C. Rioche, S. Kulkarni, F. C. Meunier, J. P. Breen and R. Burch, *Appl. Catal., B*, 2005, **61**, 130.
25 A. N. Fatsikostas, D. I. Kondarides and X. E. Verykios, *Chem. Commun.*, 2001, 851.
26 D. K. Liguras, K. Goundani and X. E. Verykios, *Int. J. Hydrogen Energy*, 2004, **29**, 419.
27 K. Hohn and Y. C. Lin, *ChemSusChem*, 2009, **2**, 927.
28 M. Scott, M. Goeffroy, W. Chiu, M. Blackford and H. Idriss, *Top. Catal.*, 2008, **51**, 13.
29 P. Y. Sheng, A. Yee, G. A. Bowmaker and H. Idriss, *J. Catal.*, 2002, **208**, 393.
30 H. Idriss, *Platinum Met. Rev.*, 2004, **48**, 105.
31 D. Wang, S. Czernik, D. Montane, M. Mann and E. Chornet, *Ind. Eng. Chem. Res.*, 1997, **36**, 1507.
32 S. Rapagnà, N. Jand and P. U. Foscolo, *Int. J. Hydrogen Energy*, 1998, **23**, 551.
33 S. Turn, C. Kinoshita, Z. Zhang, D. Ishimura and J. Zhou, *Int. J. Hydrogen Energy*, 1998, **23**, 641.
34 Y. Guo, S. Z. Wang, D. H. Xu, Y. M. Gong, H. H. Ma and X. Y. Tang, *Renewable Sustainable Energy Rev.*, 2010, **14**, 334.
35 Y. Calzavara, C. Joussot-Dubien, G. Boissonnet and S. Sarrade, *Energy Convers. Manage.*, 2005, **46**, 615.
36 Y. J. Lu, L. J. Guo, C. M. Ji, X. M. Zhang, X. H. Hao and Q. H. Yan, *Int. J. Hydrogen Energy*, 2006, **31**, 822.
37 J. R. Bolton, S. J. Strickler and J. S. Connolly, *Nature*, 1985, **316**, 495.
38 J. Lede, F. Lapicque, J. Villermaux, B. Cales, A. Ounalli, J. F. Baumard and A. M. Anthony, *Int. J. Hydrogen Energy*, 1982, **7**, 939.
39 S. Z. Baykara, *Int. J. Hydrogen Energy*, 2004, **29**, 1451.
40 D. O. Hall, M. W. W. Adams, P. Morris and K. K. Rao, *Philos. Trans. R. Soc. London, Ser. A*, 1980, **295**, 473.
41 M. Ni, K. H. Leung, D. Leung and K. Sumathy, *Renewable Sustainable Energy Rev.*, 2007, **11**, 401.
42 A. Fujishima and K. Honda, *Nature*, 1972, **238**, 37.
43 A. Kudo and Y. Miseki, *Chem. Soc. Rev.*, 2009, **38**, 253.
44 V. E. Henrich and P. A. Cox (1994) *The Surface Science of Metal Oxides*, Cambridge University Press, pp. 103 & 167.
45 J. Keeler and P. Wothers (2006) *Why Chemical Reactions Happen*, Oxford University Press, p. 61.
46 K. W. Kolasinski (2004) *Surface Science: Foundations of Catalysis and Nanoscience*, John Wiley and Sons, Ltd., p. 13 & 96.
47 W. P. Atkins and J. de Paula (2002) *Atkins' Physical Chemistry*, Oxford University Press, p. 795.
48 A. L. Linsebigler, G. Lu and J. T. Jr. Yates, *Chem. Rev.*, 1995, **95**, 735.
49 L. Kavan, M. Grätzel, S. E. Gilbert, C. Klemenz and H. J. Scheel, *J. Am. Chem. Soc.*, 1996, **118**, 6716.
50 M. Murdoch, G. I. N. Waterhouse, M. A. Nadeem, M. A. Keane, R. F. Howe, J. Llorca and H. Idriss, *Nature Chemistry*, 2011, **3**, 489.
51 W. Hebenstreit, N. Ruzycki, G. S. Herman, Y. Gao and U. Diebold, *Phys. Rev. B: Condens. Matter*, 2000, **62**, R16334.
52 X.-Q. Gong, A. Selloni, O. Dulub, P. Jacobson and U. Diebold, *J. Am. Chem. Soc.*, 2008, **130**, 370.
53 R. Hengerer, B. Bolliger, M. Erbudak and M. Grätzel, *Surf. Sci.*, 2000, **460**, 162.
54 X.-Q. Gong, A. Selloni, M. Batzill and U. Diebold, *Nat. Mater.*, 2006, **5**, 665.
55 G. von Oertzen and A. R. Gerson, *J. Phys. Chem. Solids*, 2007, **68**, 324.
56 U. Diebold, *Surf. Sci. Rep.*, 2003, **48**, 53.
57 Y. Zhang, W. Lin, Y. Li, K. Ding and J. Li, *J. Phys. Chem. B*, 2005, **109**, 19270.
58 G. I. N. Waterhouse and H. Idriss (2009) *Environmentally Benign Photocatalysts*, Springer, p. 1338.
59 H. Idriss, *Model Systems in Catalysis: From Single Crystals and Size-Selected Clusters to Supported Enzyme Mimics*, Chapter 7, Editor R. M. Rioux, Springer, 2010.
60 M. A. Barteau, *Chem. Rev.*, 1996, **96**, 1413.
61 A. K. Brisdon (1998) *Inorganic Spectroscopic Methods*, Oxford University Press, p. 58 & 74.
62 B. Jiang, J. M. Zuo, N. Jiang, M. O'Keefe and J. C. Spence, *Acta Crystallogr., Sect. A: Found. Crystallogr.*, 2003, **59**, 341.
63 S. Munnix and M. Schmeits, *Phys. Rev. B*, 1984, **30**, 2202.
64 Z. Zhang, S. Jeng and V. E. Henrich, *Phys. Rev. B: Condens. Matter*, 1991, **43**, 12004.
65 M. Calatayud, M. Markovits, B. Menetrey, B. Mguig and C. Minot, *Catal. Today*, 2003, **85**, 125.
66 S. Wang, X. Wen, D. Cao, Y. Li, J. Wang and H. Jiao, *Surf. Sci.*, 2005, **577**, 69.
67 N. Yu and J. Woods Halley, *Phys. Rev. B: Condens. Matter*, 1995, **51**, 4768.
68 O. Dulub, M. Batzill, S. Solovev, E. Loginova, A. Alchagirov, T. E. Madey and U. Diebold, *Science*, 2007, **317**, 1052.
69 J. B. Hudson (1998) *Surface Science: An Introduction*, John Wiley & Sons, Inc., p. 20.
70 B. C. Gates and H. Knozinger (2000) *Impact of surface science on Catalysis*, Academic Press, p. 263.
71 O. Dulub, C. Di Valentin, A. Selloni and U. Diebold, *Surf. Sci.*, 2006, **600**, 4407.
72 J. Matthiesen, S. Wendt, J. Hansen, G. K. H. Madsen, E. Lira, P. Galliker, E. K. Vestergaard, R. Schaub, E. Laegsgaard, B. Hammer and F. Besenbacher, *ACS Nano*, 2009, **3**, 517.
73 T. Kubo, H. Orita and H. Nozoye, *J. Am. Chem. Soc.*, 2007, **129**, 10474.
74 S. Wendt, P. T. Sprunger, E. Lira, G. K. H. Madsen, Z. Li, J. Hansen, J. Matthiesen, A. Blekinge-Rasmussen, E. Laegsgaard, B. Hammer and F. Besenbacher, *Science*, 2008, **320**, 1755.
75 N. G. Petrik, Z. Zhang, Y. Du, Z. Dohnalek, I. Lyubinetsky and G. Kimmel, *J. Phys. Chem. C*, 2009, **113**, 12407.
76 C. M. Yim, C. L. Pang and G. Thornton, *Phys. Rev. Lett.*, 2010, **104**, 036806–01.
77 C. Rohmann, Y. Wang, M. Muhler, J. Metson, H. Idriss and C. Wöll, *Chem. Phys. Lett.*, 2008, **460**, 10–12.
78 K. Mogyorosi, A. Kmetyko, N. Czirbus, G. Vereb, P. Sipos and A. Dombi, *React. Kinet. Catal. Lett.*, 2009, **98**, 215.
79 B. R. Cuenya, *Thin Solid Films*, 2010, **518**, 3127.
80 V. Subramanian, E. E. Wolf and P. V. Kamat, *J. Am. Chem. Soc.*, 2004, **126**, 4943.
81 M. Haruta, *Catal. Today*, 1997, **36**, 153.
82 M. Valden, X. Lai and D. W. Goodman, *Science*, 1998, **281**, 1647.
83 X. Lai and D. W. Goodman, *J. Mol. Catal. A: Chem.*, 2000, **162**, 33.
84 M. S. Chen and D. W. Goodman, *Top. Catal.*, 2007, **44**, 41.
85 A. Vijay, G. Mills and H. Metiu, *J. Chem. Phys.*, 2003, **118**, 6536.

86 Z. Jiang, W. Zhang, L. Jin, F. Xu, J. Zhu and W. Huang, *J. Phys. Chem. C*, 2007, **111**, 12434.
87 A. Howard, D. N. S. Clark, C. E. J. Mitchell, R. G. Edgell and V. R. Dhanak, *Surf. Sci.*, 2002, **518**, 210.
88 S. Porsgaard, P. Jiang, F. Borondics, S. Wendt, Z. Liu, H. Bluhm, F. Besenbacher and M. Salmeron, *Angew. Chem.*, 2011, **123**, 2314.
89 H. Idriss and M. A. Barteau, *Adv. Catal.*, 2000, **45**, 261.
90 H. Idriss (2008) *Handbook of Heterogeneous Catalysis Vol. 4*, ed. G. Ertl, H. Knozinger, F. Schuth, J. Weitkamp, Wiley-VCH Verlag GmbH & Co., p. 1338.
91 X. Gong, N. Khorshidi, A. Stierle, V. Vonk, C. Ellinger, H. Dosch, H. Cheng, A. Selloni, Y. He, O. Dulub and U. Diebold, *Surf. Sci.*, 2009, **603**, 138.
92 S. L. M. Schroeder, and M. Gottfried, (2002) Temperature-Programmed Desorption (TPD) Thermal Desorption Spectroscopy (TDS), available from: http://userpage.chemie.fu-berlin.de/~pcprakt/tds.pdf, [accessed 2nd June 2010].
93 P. A. Webb (2003) Introduction to Chemical Adsorption Analytical Techniques and their Applications to Catalysis, MIC Technical Publications, available from http://www.micromeritics.com/Repository/Files/intro_to_chemical_adsorption.pdf [accessed 2nd June 2010].
94 K. S. Kim and M. A. Barteau, *Langmuir*, 1988, **4**, 533.
95 J. M. Tedder And Nechvatal, (1966) *Basic Organic Chemistry, A mechanistic Approach*, John Wiley and Sons, Inc., p. 41.
96 L. Kieu, P. Boyd and H. Idriss, *J. Mol. Catal. A: Chem.*, 2002, **188**, 153.
97 R. L. Kurtz, R. Stockbauer and T. E. Madey, *Surf. Sci.*, 1989, **218**, 178.
98 M. A. Henderson, *Surf. Sci.*, 1996, **355**, 151.
99 M. B. Hugenschmidt, L. Gamble and C. T. Campbell, *Surf. Sci.*, 1994, **302**, 329.
100 P. J. D. Lindan, N. M. Harrison and M. J. Gillan, *Phys. Rev. Lett.*, 1998, **80**, 762.
101 W. S. Epling, C. H. F. Peden, M. A. Henderson and U. Diebold, *Surf. Sci.*, 1998, **412–413**, 333.
102 E. Lira, J. Ø. Hansen, P. Huo, R. Bechstein, P. Galliker, E. Lægsgaard, B. Hammer, S. Wendt and F. Besenbacher, *Surf. Sci.*, 2010, **604**, 1945.
103 W. Göpel and G. Rocker, *Phys. Rev. B*, 1983, **28**, 3427.
104 G. B. Raup and J. A. Dumesic, *J. Phys. Chem.*, 1985, **89**, 5240.
105 Z. Dohnlek, J. Kim, O. Bondarchuk, J. M. White and B. D. Kay, *J. Phys. Chem. B*, 2006, **110**, 6229.
106 T. L. Thompson, O. Diwald and J. T. Yates, *J. Phys. Chem. B*, 2003, **107**, 11700.
107 Z. Zhang and J. T. Yates, *J. Phys. Chem. C*, 2010, **114**, 3098.
108 T. L. Thompson and J. T. Yates, *J. Phys. Chem. B*, 2005, **109**, 18230.
109 T. L. Thompson and J. T. Yates, *J. Phys. Chem. B*, 2006, **110**, 7431.
110 A. Linsebigler, G. Lu and J. T. Yates, *J. Phys. Chem.*, 1996, **100**, 6631.
111 J. T. Yates, *Surf. Sci.*, 2009, **603**, 1605.
112 P. M. Jayaweera, E. L. Quah and H. Idriss, *J. Phys. Chem. C*, 2007, **111**, 1764.
113 L. Gamble, L. S. Jung and C. T. Campbell, *Surf. Sci.*, 1996, **348**, 1.
114 A. M. Nadeem, J. M. R. Muir, K. A. Connelly, B. T. Adamson, B. J. Metson and H. Idriss, *Phys. Chem. Chem. Phys.*, 2011, **13**, 7637.
115 M. A. Henderson, *J. Phys. Chem. B*, 2004, **108**, 18932.
116 M. A. Henderson, *Langmuir*, 2005, **21**, 3443.
117 M. A. Henderson, *J. Phys. Chem. B*, 2005, **109**, 12062.
118 R. T. Zehr and M. A. Henderson, *Surf. Sci.*, 2008, **602**, 2238.
119 Q. Guo, I. Cocks and E. M. Williams, *J. Chem. Phys.*, 1997, **106**, 2924.
120 Q. Guo and E. M. Williams, *Surf. Sci.*, 1999, **433–435**, 322.
121 H. Idriss, P. Legare and G. Maire, *Surf. Sci.*, 2002, **515**, 413.
122 H. Uetsuka, H. Onishi, M. A. Henderson and M. J. White, *J. Phys. Chem. B*, 2004, **108**, 10621.
123 J. N. Wilson and H. Idriss, *J. Catal.*, 2003, **214**, 46.
124 J. N. Wilson and H. Idriss, *J. Am. Chem. Soc.*, 2002, **124**, 11284.
125 J.-J. Zou, C. Chen, C.-J. Liu, Y.-P. Zhang, Y. Han and L. Cui, *Mater. Lett.*, 2005, **59**, 3437.
126 A. M. Nadeem, G. I. N. Waterhouse, J. B. Metson and H. Idriss, *Solar Hydrogen and Nanotechnology V, Book Series: Proceedings of SPIE-The International Society for Optical Engineering*, 2010, Vol. 7770..
127 Y. Wu, G. Lu and S. Li, *Mater. Lett.*, 2005, **59**, 3437.
128 C. M. Rangel, R. A. Silva, V. R. Fernandes and T. I. Paiva, *J. New Mater. Electrochem. Syst.*, 2009, **12**, 167.
129 M. C. Wu, J. Hiltunen, A. Sapi, A. Avila, W. Larsson, H. C. Liao, M. Huuhtanen, G. Toth, A. Shchukarev, N. Laufer, A. Kukovecz, Z. Konya, J. P. Mikkola, R. Keiski, W. F. Su, Y. F. Chen, H. Jantunen, P. M. Ajayan, R. Vajtai and K. Kordas, *ACS Nano*, 2011, **5**, 5025.
130 N. Strataki, N. Boukos, F. Paloukis, S. G. Neophytides and P. Lianos, *Photochem. Photobiol. Sci.*, 2009, **8**, 639.
131 G. R. Bamwenda, S. Tsubota, T. Nakamura and M. Haruta, *J. Photochem. Photobiol., A*, 1995, **89**, 177.
132 A. Tarek, A. Kandiel, L. Feldhoff, R. D. Robben and D. W. Bahnemann, *Chem. Mater.*, 2010, **22**, 2050.
133 G. I. N. Waterhouse, M. Murdoch, J. Llorca and H. Idriss, *Int. J. Nanotechnol.*, 2012, **9**, 113.
134 M. Scott, M. A. Nadeem, G. I. N. Waterhouse and H. Idriss, *Mater. Res. Soc. Proc.*, 2011, **1326**, DOI: 10.1557/opl.2011.1118.
135 M. A. Nadeem, M. Murdoch, G. I. N. Waterhouse, J. B. Metson, M. A. Keane, J. Llorca and H. Idriss, *J. Photochem. Photobiol., A*, 2010, **216**, 250.
136 G. A. M. Hossein, N. Sheppard, M. I. Zaki and R. B. Fahim, *J. Chem. Soc., Faraday Trans.*, 1991, **87**, 2661.
137 P. Y. Sheng, G. A. Bowmaker and H. Idriss, *Appl. Catal., A*, 2004, **261**, 171.
138 V. Blagojevic, Y. R. Chen, M. Steigerwald, L. Brus and R. A. Friesner, *J. Phys. Chem. C*, 2009, **113**, 19806.
139 M. J. Lundkvist, M. Nilsing, P. Persson and S. Lunell, *Int. J. Quantum Chem.*, 2006, **106**, 3214.
140 B. R. Miller, S. Majoni, R. Memming and D. Meissner, *J. Phys. Chem. B*, 1997, **101**, 2501.
141 J. Zhang, Q. Xu, Z. Feng, M. Li and C. Li, *Angew. Chem., Int. Ed.*, 2008, **47**, 1766.
142 D. C. Hurum, K. A. Gray, T. Rajh and M. C. Thurnauer, *J. Phys. Chem. B*, 2005, **109**, 977.

